

# Lawrence Berkeley National Laboratory

## Recent Work

### Title

FLUID FLOW PATTERNS AND SOLVENT SELECTION FOR LIQUID PHASE EPITAXIAL CRYSTAL GROWTH ON ROTATING CRYSTALS

### Permalink

<https://escholarship.org/uc/item/7200k96c>

### Author

Chen, Pei-Shiun.

### Publication Date

1974-12-11

FLUID FLOW PATTERNS AND SOLVENT SELECTION FOR  
LIQUID PHASE EPITAXIAL CRYSTAL GROWTH  
ON ROTATING CRYSTALS

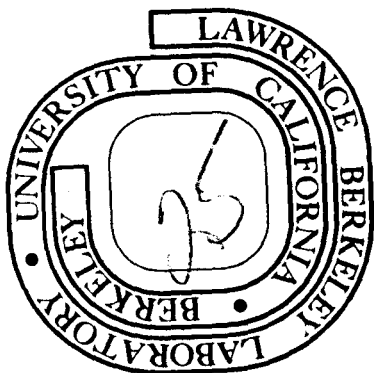
Pei-Shiun Chen  
(M. S. thesis)

December 11, 1974

Prepared for the U. S. Atomic Energy Commission  
under Contract W-7405-ENG-48

TWO-WEEK LOAN COPY

*This is a Library Circulating Copy  
which may be borrowed for two weeks.  
For a personal retention copy, call  
Tech. Info. Division, Ext. 5545*



## **DISCLAIMER**

This document was prepared as an account of work sponsored by the United States Government. While this document is believed to contain correct information, neither the United States Government nor any agency thereof, nor the Regents of the University of California, nor any of their employees, makes any warranty, express or implied, or assumes any legal responsibility for the accuracy, completeness, or usefulness of any information, apparatus, product, or process disclosed, or represents that its use would not infringe privately owned rights. Reference herein to any specific commercial product, process, or service by its trade name, trademark, manufacturer, or otherwise, does not necessarily constitute or imply its endorsement, recommendation, or favoring by the United States Government or any agency thereof, or the Regents of the University of California. The views and opinions of authors expressed herein do not necessarily state or reflect those of the United States Government or any agency thereof or the Regents of the University of California.

Table of Contents

ABSTRACT . . . . .	v
I. GENERAL INTRODUCTION . . . . .	1
REFERENCES . . . . .	3
II. VISCOUS FLUID FLOW DURING CRYSTAL GROWTH IN ROTATING SYSTEM . . . . .	4
A. Introduction . . . . .	4
B. Theory . . . . .	6
1. Flow Between Coaxial Disks . . . . .	7
2. Flow to a Finite Rotating Disk . . . . .	9
3. Flow Instability . . . . .	10
4. Edge Effects . . . . .	11
5. Dimensionless Groups . . . . .	12
C. Experimental . . . . .	13
1. Apparatus . . . . .	13
2. The Working Fluid . . . . .	14
3. Procedure . . . . .	14
D. Experimental Results . . . . .	16
E. Discussion . . . . .	19
FIGURE CAPTIONS . . . . .	23
FIGURES . . . . .	26
REFERENCES . . . . .	34

III. SOLVENT SELECTION FOR CONGRUENT SATURATION OF MAGNETIC GARNETS . . . . .	36
A. Introduction . . . . .	36
B. Phase Equilibria . . . . .	38
FIGURE CAPTIONS . . . . .	43
FIGURES . . . . .	44
REFERENCES . . . . .	46
IV. AN EXPERIMENTAL STUDY OF THE $\text{PbO-BaO}\cdot\text{B}_2\text{O}_3$ SOLVENT SYSTEM FOR CONGRUENT SATURATION AND LIQUID PHASE EPITAXIAL GROWTH OF $\text{EuEr}_2\text{Fe}_{4.3}\text{Ga}_{0.7}\text{O}_{12}$ FILMS . . . . .	47
A. Introduction . . . . .	47
B. Experimental Apparatus and Method . . . . .	51
D. Discussion and Conclusions . . . . .	62
FIGURE CAPTIONS . . . . .	64
FIGURES . . . . .	65
REFERENCES . . . . .	72
V. GENERAL CONCLUSION . . . . .	73
ACKNOWLEDGEMENTS . . . . .	74
APPENDIX . . . . .	75
FIGURE CAPTIONS . . . . .	80
FIGURES . . . . .	81
LIST OF SYMBOLS . . . . .	87

FLUID FLOW PATTERNS AND SOLVENT SELECTION  
FOR LIQUID PHASE EPITAXIAL CRYSTAL GROWTH  
ON ROTATING CRYSTALS

Pei-Shiun Chen

Inorganic Materials Research Division, Lawrence Berkeley Laboratory  
and Department of Chemical Engineering; University of California  
Berkeley, California

ABSTRACT

Fluid flow conditions and thermochemical properties of solvent systems were studied for solution crystal growth in rotating systems. Fluid flow patterns were studied with time-lapse photography using the dye-tracer method for flow delineation. Simulation of solution crystal growth and Czochralski crystal growth revealed that the convection currents induced by crystal rotation in a stationary and slowly co-rotating crucible provided the best mixing conditions at the crystallization interface. The boundary layer beneath the crystal became more uniform and thinner as the crystal rotation rate increased. The dimensions of the crystal boundary-layer cell and overall mixing rates were reduced by counterrotation of the crucible. The overall convective mixing rate was lowest for co-rotation of the crystal and crucible with comparable angular velocities.

The mixed solvent system  $\text{PbO}_x(\text{BaO} \cdot \text{B}_2\text{O}_3)_{1-x}$  was investigated theoretically and experimentally for conditions allowing congruent saturation of rare-earth magnetic garnets and efficient liquid phase epitaxial growth. High quality  $\text{Eu}_1\text{Er}_2\text{Ga}_{0.7}\text{Fe}_{4.3}\text{O}_{12}$  films were obtained from solvents containing 10 mole % garnet oxides.

## I. GENERAL INTRODUCTION

The widespread use of liquid phase epitaxy for the growth of single crystal films has been encumbered by three major difficulties. First, there is the tendency towards polycrystallite growth by multiple nucleation when the supersaturation is not constrained. Second, solvent inclusions frequent occur within crystals grown at high rates.<sup>1</sup> Thirdly, the non-congruency of melts used for garnet crystal growth can cause the deposition of unwanted phases as the growth process continues.<sup>2</sup> The first problem can generally be solved by controlled seeding.<sup>3</sup> To reduce the second problem, stirring has a beneficial effect in preventing inhomogeneous supersaturation along the crystallization interface. Scheel found that stirring is an important way to obtain solvent-inclusion free growth.<sup>4</sup> The third problem can be overcome by using an appropriate melt composition. Quon showed that suppression of an orthoferrite phase during solution growth of garnets could be achieved by increasing both the iron oxide and gallium oxide content above the stoichiometric mole fraction required.<sup>5</sup> In this thesis, two problems were chosen for study: the fluid flow patterns produced by crystal or crucible rotation, and solvent systems for optimizing the crystal yield by solution growth.

The rotation of crystals during crystal growth is a frequently used method for stabilizing convective mass transfer during controlled crystal growth from the melt as in the Czochralski process and from solution as for liquid phase epitaxial (LPE) crystal growth.<sup>6</sup> The important effect derived from the rotation of planar crystallization

interfaces is that a hydrodynamic boundary layer of uniform thickness is stabilized over the surface. In this study the effect of rotation on fluid flow is examined by simulation experiments.

The recent development of magnetic, antiphase domain "bubble" memory devices with rare-earth magnetic garnet films has induced extensive research and development into the magnetic bubble phenomenon and the processing of magnetic bubble memory devices. Unfortunately, the problem of solvent selection for optimal saturation and growth of the garnet phase has received relatively little study. All of the solvent systems used to date for LPE growth of magnetic garnet films are non-congruently saturating. Since a congruently saturating solvents will extend the yield efficiency in a given solution growth process and prevent secondary phases from precipitating, a study of solvent systems is essential to economic process design. In this thesis, the LPE growth of  $\text{EuEr}_2\text{Ga}_{0.7}\text{Fe}_{4.3}\text{O}_{12}$  from solvents of the system  $\text{PbO}_x(\text{BaO} \cdot \text{B}_2\text{O}_3)_{1-x}$  is studied for conditions allowing congruent saturation of the garnet phase.

REFERENCES

1. H. L. Glass, Mat. Res. Bull. 7, 385 (1972).
2. L. J. Varneria, "A Perspective on Magnetic Materials for Bubble Mass Memories" presented at the 1972 Intermag. Conference, Kyoto, Japan.
3. V. Belruss, J. Kalnays, A. Liry and R. C. Folweiler, Mat. Res. Bull. 6, 899 (1971).
4. H. J. Scheel and D. Elwell, J. of Electrochem. Soc. 120, 818 (1973).
5. H. H. Quon and A. J. Potvin, Mat. Res. Bull. 7, 463 (1972).
6. R. Ghez and E. A. Giess, Mat. Res. Bull. 8, 31 (1973).

## II. VISCOUS FLUID FLOW DURING CRYSTAL GROWTH IN ROTATING SYSTEM

### A. Introduction

The hydrodynamics of viscous fluid flow under conditions of forced and thermally driven convection are known to affect crystal growth processes. Mixing conditions contribute significantly to the crystal growth rate, mass redistribution, dislocation density, faceting effects and composition inhomogeneities in many crystal growth processes. These effects are particularly evident in growth methods involving rotation of the crystal or fluid, as in the Czochralski crystal growth process where a rotating crystal is pulled from the melt, and in solution crystal growth in rotating crystallizers.

The effect of convective fluid flow produced by crystal or crucible rotation on crystal growth processes has become an important area for both theoretical and experimental study in the last decade. Many studies of the best known rotational growth method, the Czochralski growth process, have shown a dependence of periodic composition variation on thermal convection and its effect on the temperature distribution at the crystal-melt interface.<sup>1-7</sup> Striation effects in crystals have been reviewed by Muller and Wilhelm who showed that the spacing between Te-impurity striations correlated with the frequency of thermal oscillations in the melt.<sup>2</sup> Komarov and Regel have observed periodic growth and remelting of bismuth produced by turbulent thermal convection.<sup>3</sup> Not all of the striation effects are produced by convection, as helical growth striations in rotated, Czochralski-grown crystals

have since been shown to be induced by non-axially symmetric thermal gradients in the melt.<sup>4-6</sup> Benson has shown that stirring conditions contribute markedly to radial macrosegregation in Czochralski-grown silicon.<sup>7</sup>

Schulz-DuBois<sup>8</sup> and Hurle<sup>9</sup> have both pointed out that crucible rotation can produce drastic influences in the hydrodynamic conditions of the solution crystal growth processes. Scheel<sup>10</sup> has used an accelerated crucible-rotation technique to increase the rate of mass transfer and thermal equilibration for solution crystal growth of  $GdAlO_3$  from  $PbO-PbF_2-B_2O_3$  solvents.

The direct observation of fluid flow has recently been shown to provide valuable information about mixing conditions and fluid velocities in the liquid phase. Flow tracing<sup>11</sup> has been studied by many methods including dye tracing,<sup>12</sup> optical interference<sup>13</sup> and optical scattering.<sup>14</sup> Dye-tracer delineation of flow in transparent fluids is an excellent method for simulating crystal growth in rotating systems. This method has been applied to Czochralski crystal growth simulation,<sup>15-19</sup> but has been limited to low viscosity liquids. This method however, can easily be extended to liquids of higher viscosity. Thus, further study of this hydrodynamics of viscous fluid flow in crystal growth processes is desirable.

In this study the fluid flow pattern in viscous fluids are studied in an isothermal system consisting of a fluid-filled crucible with an axially-symmetric planar crystal at the upper liquid surface. This

geometry simulates nearly isothermal Czochralski crystal growth as well as liquid phase epitaxial growth on rotating disk substrates. Finite-viscosity effects are introduced by using ethylene glycol as the working fluid. The thermal gradients present in the Czochralski growth process were omitted from the simulation as earlier studies have shown that thermal convection does not dominate the forced convection.

### B. Theory

Simulations of fluid motion during Czochralski and solution crystal growth fall into a first class of rotating fluid motion problems in hydrodynamic theory where the fluid is enclosed within bounding surfaces which are the significant cause of the fluid motion. The problem of fluid motion during epitaxial growth on rotating substrates falls into a second class of problems where the influence of outer bounding walls is only of secondary importance in influencing fluid motion compared with the effect of the rotational motion of the immersed substrate. The simplest theorem which can qualitatively describe the convective motions in rotating liquid is the Taylor-Proudman theorem.<sup>20,21</sup> Taylor first successfully treated the rotating fluid problem by theoretical and experimental means. This famous theorem states that all steady motions in a rotating fluid are two-dimensional with respect to the rotating axis. The Taylor-Proudman theorem is only strictly valid for fluids with zero viscosity, but the theorem is approximately valid at sufficiently high Reynolds number. The Reynolds number is defined by

$$N_{Re} = \frac{L^2 \Omega}{\nu} \quad (1)$$

where  $L$  is the depth of fluid between crystal and crucible,  $\nu$  is the kinematic viscosity, and  $\Omega$  is a rotational angular velocity. In this study the Reynolds number ranged from 20.83 to 125.0 and the Taylor-Proudman theorem is expected to hold. In problems of viscous flow in fluids between parallel rotating disks, the characteristic parameters are the disk radius  $R_1$ , the crucible radius  $R_2$  and their angular rotation velocities  $\Omega_1$  and  $\Omega_2$ .

We may consider a first class of problems as the case of fluid flow between coaxial disks of finite extent. Here the crucible walls play a significant role in influencing flow velocity distributions. In a second class of problems, the fluid flow is to a finite rotating disk, and other boundary surfaces are of limited significance.

#### 1. Flow Between Coaxial Disks

The bounded flow between finite, rotating disks differs substantially from that for the unbounded flow problem. The problem of the steady fluid flow of a viscous, incompressible fluid between coaxial disks separated by a distance  $L$  has inspired attention because of the possibility of solving the Navier-Stokes equations exactly for any Reynolds number. As the Reynolds number  $N_{Re}$  increases, boundary layers form adjacent to the rotating surfaces with thickness  $\delta \propto N_{Re}^{-1/2}$ . Bachelor argued that the fluid outside the surface boundary layers would not approach the von Kármán free-disk solution, but would rotate

with a constant angular velocity,  $\Omega_f$  and that boundary layers would develop on both disks.<sup>22</sup> Although Stewartson argued differently on the basis of trends at low Reynolds number, the numerical solutions of Lance and Rogers,<sup>23</sup> Pearson<sup>24</sup> and Stephenson<sup>25</sup> show that Bachelor's qualitative picture of the flow is essentially correct.

Fluid flow in idealized configurations containing finite, coaxial disks have been the subject of several experimental studies utilizing either gases or liquids as the working fluid. Schulz-Grunow,<sup>26</sup> Picha and Eckert<sup>27</sup> and Stewartson<sup>28</sup> studied fluid flow between centered disks of equal, but finite, size in an open fluid. When only one disk was rotated at a constant rate while the other was stationary, the main body of fluid between the disks remained essentially quiescent. The main fluid motion was within the boundary layer on the rotating disk, but there was little motion elsewhere.

Picha and Eckert also studied fluid flow between finite, coaxially rotating disks shrouded by a closely fitting cylindrical container.<sup>27</sup> This configuration closely resembles the Czochralski crystal growth configuration utilized in the present study. Again, when only one disk was rotated at a constant rate, the observed fluid motion within the cylinder closely resembles the flow between infinite plates, except that the azimuthal flow velocity over most of the central core was only about three-tenths that of the rotating disk. Their experimental results for counter-rotating disks bounded laterally by a stationary cylinder showed no circular motion of the internal fluid.

Carruthers and Nassau described the forced convection induced by crystal and crucible rotation in a simulated Czochralski crystal growth system using a transparent liquid of low viscosity with injected dye.<sup>29</sup> These authors also observed detached shear layers in the fluid when the crystal and crucible were counter rotated. It is evident that shear layers play an important role in rotational crystal growth processes, and that their magnitude and effect should increase with increasing viscosity of the crystallizing fluid.

## 2. Flow to a Finite Rotating Disk

Hyde and Titman studied the detached shear layers in a system in which fluid filling a rotating cylindrical container is stirred by a disk immersed in the fluid.<sup>30</sup> They found that there was a non-axisymmetric shear layer formed when the Rossby number was greater than a critical value. Outside the shear layers, an axial velocity component is required to balance radial flow within the shear layer. To determine the axial velocity, consider a disk of radius  $R_1$  rotating with velocity  $\Omega$ . The flow to the boundary layer must equal the radial flow through the annulus of thickness  $\delta$  with the average radial velocity given by  $\bar{v}_r = 0.424r\Omega$ . The axial velocity which balances the radial flow is then

$$v_z \Big|_{z=\delta} = 0.8856 \sqrt{\gamma\Omega} \quad (2)$$

Therefore, the axial velocity depends on the angular velocity of the disk, but not on its radius. Similar estimates can be made for axial flow to detached shear layers. The fluid motion near a slow, axially

moving disk in a viscous, rotating fluid has been studied by Morrison and Morgan using transform methods.<sup>31</sup> The axial flow velocity then depends also on the axial velocity of the disk.

### 3. Flow Instability

The Rayleigh criterion for stable, rotational flow indicates the limits of stability. In the absence of viscosity the necessary and sufficient condition for angular velocity distribution to go unstable is

$$\frac{d}{dr} N_T = \frac{d}{dr} (r^2 \Omega)^2 < 0 . \quad (3)$$

The Rayleigh criterion for  $v=0$  therefore states that for stable flow the angular momentum per unit mass,  $|r^2 \Omega|$ , must not decrease with increasing radius, with the instability limit given by

$$\mu = \frac{\Omega_2}{\Omega_1} \geq \left( \frac{R_2}{R_1} \right)^2 = \rho^2, \text{ (stable flow)} \quad (4)$$

For flow stability on the surface liquid then, the crystal must rotate in the same direction as the crucible (co-rotation), but with angular velocity  $(R_2/R_1)^2$  times that of the crucible. When the crystal and crucible rotate in opposite directions (counter-rotation), the surface flow is unstable for radii less than the model plane radius  $R_0$  given by and stable for radii larger than  $R_0$ .

$$R_0 = (r_2 - r_1) / (r_2 R_1^{-2} - r_1 R_2^{-2}) \quad (5)$$

The effect of finite fluid viscosity is to postpone the onset of flow instability by viscous dissipation. The instability criterion was first explored by G. I. Taylor who found an analytical expression for the criterion.<sup>20</sup> The results show that for  $\Omega_1$  less than a minimum value the flow is stable for all values of  $\Omega_2$ . As  $\Omega_1$  increases above the minimum value, the flow becomes unstable for an increasingly wide range of both positive and negative values.

#### 4. Edge Effects

Edge effects on fluid flow to rotating surfaces are often neglected on the assumption that such effects have negligible influence on fluid flow near the axis of rotation, provided that the boundary layer thickness is much less than the surface radius. The values of  $v_r$  and  $v_\theta$  are nevertheless proportional to  $r$ , according to the similarity transformation, and therefore the radial and tangential momenta are most sensitive to defects in the rotating surface and to discontinuities in stress on the fluid at the surface edge. The edge discontinuity is more pronounced for inward flow than for outward flow on the surface since in an outward flowing layer the flow is stabilized by the flow field established at small radii. For an inward flowing layer where the flow field is controlled at large radii the stability of the flow may be difficult to achieve. It follows from the Raleigh criterion that unstable flow will occur around the edge of the rotating surface if the inequality  $\partial(r^2\Omega)^2/\partial r < 0$  is fulfilled. In general the edge effects are complex and not easily handled analytically.

## 5. Dimensionless Groups

Theoretical properties of fluid flow and of flow stability are often most conveniently expressed in terms of non-dimensional numbers, or groups, the most famous of which is the Reynolds number,\* given in Eq. 1. In problems of viscous flow in fluids between parallel rotating disks, the parameters are the disk radius  $R_1$ , the crucible radius  $R_2$  and their angular rotation velocities  $\Omega_1$  and  $\Omega_2$ . The dimensionless groups of these parameters and physical constants are then

$$\rho = \frac{R_2}{R_1}, \quad \sigma = \frac{L}{R_1}, \quad \mu = \frac{\Omega_2}{\Omega_1}. \quad (6)$$

A dimensionless group which always appears in rotating systems is the Taylor number,

$$N_T = \frac{4\Omega^2 R^4}{\nu^2}$$

in which  $R$  is any of the linear dimensions. The vorticity of the basic rotation, is measured by the Rossby number defined by

$$N_R = \frac{\Omega_1 - \Omega_2}{\frac{1}{2}(\Omega_1 + \Omega_2)} \quad (7)$$

These variables are used in evaluating the experimental results which follow.

---

\* Symbols are defined at the end of the thesis.

### C. Experimental

#### 1. Apparatus

Experiments were designed to simulate Czochralski crystal growth from viscous melts, and liquid phase epitaxy of garnet films from solution on rotating substrates. Flow patterns were delineated by the dye tracer method and time-lapse photography. The simulation apparatus of Fig. 3 consisted of a 96 mm inner dia. cylindrical beaker and polymethylmethacrylate simulation-crystal cylindrical solids, aligned coaxially and independently driven by variable speed synchronous motors. The diameters of the simulation crystals used were 32 mm( $\rho=3$ ) and 48 mm( $\rho=2$ ).

Studio lamps were placed behind opaque screens surrounding the crucible to illuminate the fluid. A digital timer was reflected into the viewing area by a small mirror placed below the crucible. The timer was reset for each experiment to indicate the time interval following dye injection in the time-lapse photographs. The depth of the ethylene glycol working fluid could be adjusted, but the simulation crystal was placed in contact with and parallel to the upper surface of the fluid.

For flow visualization the angular velocities of the crucible and simulation crystal were fixed, and the forced convection in the fluid allowed to reach steady state. Then a neutrally bouyant dye dissolved in ethylene glycol was injected with a 0.5 mm capillary syringe into the fluid at the center of the simulation-crystal disk surface, or alternately at other points within the fluid. The dye-traced flow was then

photographed by time-lapse, 35 mm photography. To allow correction for the lens effect of the cylindrical crucible, a mirror was positioned over the melt at an angle of  $45^\circ$  to the vertical in order to allow simultaneous viewing from the top and side. A red filter was used to enhance the contrast between the aniline blue dye and the background. Other dyes examined were found to provide lower contrast. A frame of reference was established for the rotating crucible by synchronizing the interval between photographs to the crucible or crystal rotation speed, and by setting the ratio of crucible and crystal rotation speeds equal to the ratio of small integers.

## 2. The Working Fluid

Ethylene glycol is found to exhibit excellent physical properties for simulation of viscous fluid flow during crystal growth. Its kinematic viscosity is considerably higher than that of the water and water-glycerol mixtures studied earlier in simulation experiments. The physical properties of ethylene glycol are summarized in Table 1. Because it contains a single component, the problem of incomplete mixing in water-glycerine mixtures is avoided. Also, because of the higher viscosity, the thickness of the hydrodynamic boundary layers,  $\delta$  given by Eq. 9 becomes observably large at experimentally convenient angular velocities.

## 3. Procedure

The following steps were used in each experiment. The crucible was filled to the desired height with ethylene glycol. The simulation crystal was then lowered to a height sufficient for contact with the

Table 1. Physical Properties of Ethylene Glycol<sup>35</sup> (1,2-Ethanediol, HOCH<sub>2</sub>CH<sub>2</sub>OH).

Property		Temperature	
		20°C	40°C
Density	$d(\text{gm/cm}^3)$	1.113	1.099
Kinematic viscosity	$\nu(\text{cm}^2/\text{sec})$	0.1915	0.0879
Specific heat	$C_v(\text{ergs/gm}^\circ\text{C})$	$2.38 \times 10^7$	$2.48 \times 10^7$
Thermal diffusivity	$\kappa(\text{cm}^2/\text{sec})$	$9.42 \times 10^{-4}$	$9.42 \times 10^{-4}$
Coefficient of thermal expansion	$\alpha(^\circ\text{C}^{-1})$	$6.4 \times 10^{-3}$	$6.5 \times 10^{-3}$

rotating fluid after  $\Omega_1$  and  $\Omega_2$  had been set. The system was allowed to reach complete steady state, then dye was injected at a fixed point and the digital timer started. Photographs of the dye traces were then taken at regular time intervals. Experiments were conducted to define fluid flow patterns under conditions of i) counter-rotation of crystal and crucible, ii) crystal rotation only, and iii) co-rotation of crystal and crucible.

#### D. Experimental Results

Initial experiments were designed to study fluid flow velocities during the simulated Czochralski or solution crystal growth under isothermal conditions. Several different conditions of rotation were studied. Rotation rates of the simulation crystal and crucible were set at 15 r.p.m. intervals between -90 r.p.m. and 90 r.p.m.

The results of dye-traced flow experiments with  $\rho=R_2/R_1=3$  and  $\sigma=L/R_1=2$  are shown in Fig. 4. In each experiment the dye was injected at the center of the simulation crystal face. For counter-rotation with crystal rotation controlling the flow, the dye remained within a fluid layer adjacent to the simulation crystal. For counter-rotation with crucible rotation controlling the flow, the dye trace moved downward with a gradually accelerating rate to the bottom surface of the crucible, where it spread outward in the radial direction by centrifugal force, then upward. At the wall of the crucible the fluid was almost stagnant.

For crystal rotation only, the dye spread outward in the radial direction by centrifugal force, then descended gradually. The central part of the fluid between the crucible and crystal formed a torus-shaped vortex ring.

Co-rotation of the crystal and crucible produced a modification of the simple flow for crucible rotation only. When the rotation rate of the crystal was large, the flow pattern was similar to that for crystal rotation only. When the rotation rate of the crystal was smaller than that of the crucible, then the flow pattern was nearly solid body rotation. The dye motion was then limited to a small axial region just underneath the center of the crystal.

Additional experiments were performed to determine the effect of the variables  $\rho$ ,  $\sigma$  and  $\mu$  on shear layers and forced convection velocities. The fluid flow patterns for crystal rotation only are shown in Fig. 5. The fluid in the center of the crucible rotated in a torus-shaped vortex ring in all experiments. When the rotation rate was small, the radius of the vortex ring was correspondingly small, as was the circulation velocity. When the rotation rate was increased to 90 r.p.m., the axis radius of the vortex ring expanded to a value equal to the radius of the crystal, and the nearly stationary fluid region at the crucible wall became smaller. The forced convection flow then reached almost every part of the vessel.

Flow patterns for crucible rotation only are shown in Fig. 6. At low crucible rotation rates the dye trace was close to the crucible wall, and the shear boundary layer next to the crystal was nonuniform.

There was a small vortex just beneath the edge of the crystal. For faster rotation rates the flow velocity was higher and the vortex ring became a cylinder whose radius was near that of the crystal.

Flow patterns for co-rotation are shown in Fig. 7. combinations of crystal and crucible rotation in the same sense produced a modification of the simple flow pattern for crucible rotation only. Couette instability was observed to occur when the crystal rotation velocity was much higher than that of the crucible. When the rotation rate of the crystal was smaller than that of the crucible the induced flow pattern was confined to a cylinder directly underneath the crystal, and the flow was stable against Couette instability. When the rotation rates of both crucible and crystal were the same, the fluid rotated as a solid body. The degree of mixing for co-rotation was very low.

Flow patterns for counter-rotation of the crystal crucible are shown in Figs. 8 and 9. The circulation influenced by the crystal and crucible were always separated by a stagnant surface. Therefore, the whole fluid could be divided into three parts: i) the crystal-influence region, ii) the crucible-influence region, and iii) a solid body rotation region at the upper part of the crucible wall. For  $\Omega_1 > -\Omega_2$  the flow pattern was similar to that for crystal rotation only, except that this region was much smaller and limited to a region just beneath the crystal. Several vortices could be seen on the fluid surface for some ranges of rotation rates with  $\Omega_1 > -\Omega_2$ . When the crucible rotation rate increased, this region decreased to negligible size.

### E. Discussion

For most liquid metals the viscosity at the melting temperature is small, 1-4 cp. Thus, there is a thin boundary layer at the crucible wall and beneath the crystal bottom face. The thickness of these boundary layers is so thin that rotation produces negligible fluid flow.

In crystal growth from solution, on the other hand, the viscosity of the solution can be large, and mass transfer from solution through a larger boundary layer to the solid phase is required. The crystallizing component moves from the bulk solution to the boundary layer by convection, then diffuses through the boundary layer to the surface of the crystal. Latent heat of crystallization is released at the surface. Therefore, the purpose of crystal and crucible rotation is i) to reduce the thickness of the boundary layers, and ii) to increase the mixing regions throughout the entire vessel by circulation of the fluid. The mixing circulation generally increased with  $N_R$ .

A comparison between the experimentally observed flow patterns and those for low viscosity fluids is shown in Fig. 10. The flow patterns observed in ethylene glycol, representing a viscous crystal growth solution, differed significantly from the flow predicted for an inviscid fluid. Detached shear layers were observed below the simulation crystal.

For crystal rotation only, a detached shear layer was expected to form along a cylinder below the crystal. Instead, the shear layer was a flared conic with a radius which increases with distance from the crystal. Therefore the flow pattern in this case could be divided into three parts,

- i) a central cone in solid body rotation rising toward the crystal,
- ii) a vortex ring circulating below the crystal outer radius, and
- iii) a stagnant boundary layer adjacent to the crucible outer wall.

When the crystal rotation rate was increased, the width of the shear layer and of the boundary layer adjacent to the crucible wall decreased in reasonable agreement with the angular velocity dependence of Eq. 9.

For crucible rotation only, the detached shear layer remained cylindrical, with a radius approximately that of the crystal, for all rotation rates. There was a slight vortex just beneath the edge of the crystal, however. A similar flow pattern was found for co-rotation. The mixing for these rotation conditions was very poor.

For counter-rotation, the flow pattern in the region influenced by the crystal is similar to the case of crystal rotation only, except that this region is smaller and limited to a small volume underneath the crystal. The thickness of this region varied with the radial distance from the axis of rotation. As the magnitude of the crystal rotation rate was increased above that of the crucible the crystal-influenced region became wider and thicker and the rate of change of thickness with radial distance changed sign with increasing crystal rotation rate. Instabilities were observed on the surface of the liquid in the form of asymmetric surface vortices, appearing in modes of equispaced groups of two, three or four. The modes depended on the rotation rates, but the systematic dependence was not identified.

The rates of flow circulation were studied for the dependence on rotation rates of the the crucible and simulation crystal. The general dependence of the axial flow velocity increased with  $\Omega_2^{1/2}$ , in accordance with Eq. 11.

Rotating the crucible by an accelerated-decelerated technique is an effective method to achieve composition uniform in these solutions. From experiments it was found that the time to reach homogeneity by this method is about one-third of the homogenization time by the conventional rotating crucible method. This phenomena can be simply interpreted by hydrodynamic principles. When an incompressible fluid is caused to decrease its speed of flow there is an increase in pressure and vice versa. Any change in velocity profile will also cause a change of pressure. A pressure gradient is then built up. This pressure gradient will induce a mass transfer by pressure diffusion. When the crucible was suddenly stopped, the fluid closed to the solid walls was stopped immediately, but the bulk liquid still had a large angular momentum. The pressure is higher at solid boundaries and is lower at the center. Fluid then flows from outside to the center and upwards. The flow direction is just opposite to the regular flow pattern which is caused by constant rotating crucible.

When the rotation speed was high gas bubbles were produced which attached to the crystal surface. Higher rotation speeds produced higher numbers of bubbles with a smaller size. This effect tends to produce cavities in real crystals during the growth process. Because the center of the rotating crystal is a stagnant point and a bubble attached to that point will be stabilized by the centripetal force field and the surface tension.

The stability at higher angular velocity is lower (producing fluctuation of motion and bubbles) but the time to reach homogeneity is shorter. Thus, there must be an optimum rotation speed for each system. System with higher viscosity usually will have higher critical rotation speed to keep stable motion.

FIGURE CAPTIONS

Fig. 1. Fluid velocity functions F, G and H. (after von Kármán<sup>20</sup>).

Fig. 2. Axial fluid velocity to a disk rotating with angular velocity  $\Omega_1$  from a co-rotating fluid with bulk angular velocity  $\Omega_f$  (after Rogers and Lance<sup>23</sup>).

Fig. 3. Schematic of Apparatus used for flow visualization.

Fig. 4. Dye-traced fluid flow simulating crystal growth in rotating systems =  $\rho = 3$ ,  $\sigma = 2$ .

- I. Counter-rotation with crystal-rotation control of flow,  $\Omega_1 = 6.28 \text{ sec}^{-1}$ ,  $\Omega_2 = -1.57 \text{ sec}^{-1}$  for time = 6.9 sec (a), 11.7 sec (b), 18.6 sec (c), 29.3 sec (d), 63.4 sec (e).
- II. Counter-rotation with crucible rotation control of flow,  $\Omega_1 = 1.57 \text{ sec}^{-1}$ ,  $\Omega_2 = -3.14 \text{ sec}^{-1}$  for time = 5.2 sec (a), 17.4 sec (b), 25.3 sec (c), 42.3 sec (d), 80.0 sec (e).
- III. Crystal rotation only,  $\Omega_1 = 3.14 \text{ sec}^{-1}$ ,  $\Omega_2 = 0$ . for time = 7.0 sec (a), 61.5 sec (b), 120 sec (c), 170 sec (d), 210 sec (e).
- IV. Co-rotation with crystal-rotation control of flow,  $\Omega_1 = 6.28 \text{ sec}^{-1}$ ,  $\Omega_2 = 1.57 \text{ sec}^{-1}$  for time = 5.7 sec (a), 15.0 sec (b), 34.0 sec (c), 62.5 sec (d), 130.4 sec (e).
- V. Co-rotation with crucible-rotation control of flow,  $\Omega_1 = 1.57 \text{ sec}^{-1}$ ,  $\Omega_2 = 6.28 \text{ sec}^{-1}$ . for time = 7.2 sec (a), 16.3 sec (b), 85.4 sec (c), 256.5 sec (d), 420.7 sec (e).

Fig. 5. Dye-traced fluid flow with crystal rotation only.

- a)  $\Omega_1 = 3.14 \text{ sec}^{-1}$ ,  $\rho=3$ ,  $\sigma=2$ ; b)  $\Omega_1 = 6.28 \text{ sec}^{-1}$ ,  $\rho=3$ ,  $\sigma=2$ ;  
c)  $\Omega_1 = 3.14 \text{ sec}^{-1}$ ,  $\rho=2$ ,  $\sigma=2$ ; d)  $\Omega_1 = 1.57 \text{ sec}^{-1}$ ,  $\rho=3$ ,  $\sigma=3$ ;  
e)  $\Omega_1 = 6.28 \text{ sec}^{-1}$ ,  $\rho=3$ ,  $\sigma=3$ ; f)  $\Omega_1 = 7.85 \text{ sec}^{-1}$ ,  $\rho=3$ ,  $\sigma=3$ .

Fig. 6. Dye-traced fluid flow with crucible rotation only.

- a)  $\Omega_2 = 1.57 \text{ sec}^{-1}$ ,  $\rho=3$ ,  $\sigma=2$ ; b)  $\Omega_2 = 1.57 \text{ sec}^{-1}$ ,  $\rho=3$ ,  $\sigma=3$ ;  
c)  $\Omega_2 = 3.14 \text{ sec}^{-1}$ ,  $\rho=2$ ,  $\sigma=2$ ; d)  $\Omega_2 = 3.14 \text{ sec}^{-1}$ ,  $\rho=3$ ,  $\sigma=3$ ;  
e)  $\Omega_2 = 4.71 \text{ sec}^{-1}$ ,  $\rho=3$ ,  $\sigma=3$ ; f)  $\Omega_2 = 6.28 \text{ sec}^{-1}$ ,  $\rho=3$ ,  $\sigma=3$ .

Fig. 7. Dye-traced fluid flow with co-rotating crystal and crucible.

$\rho=3$ ,  $\sigma=3$ .

- a)  $\Omega_1 = 4.71 \text{ sec}^{-1}$ ,  $\Omega_2 = 3.14 \text{ sec}^{-1}$ ; b)  $\Omega_1 = 4.71 \text{ sec}^{-1}$ ,  $\Omega_2 = 1.57 \text{ sec}^{-1}$ ,  
c)  $\Omega_1 = 6.28 \text{ sec}^{-1}$ ,  $\Omega_2 = 1.57 \text{ sec}^{-1}$ ; d)  $\Omega_1 = 1.57 \text{ sec}^{-1}$ ,  $\Omega_2 = 3.14 \text{ sec}^{-1}$ ,  
e)  $\Omega_1 = 1.57 \text{ sec}^{-1}$ ,  $\Omega_2 = 4.71 \text{ sec}^{-1}$ ; f)  $\Omega_1 = 1.57 \text{ sec}^{-1}$ ,  $\Omega_2 = 6.28 \text{ sec}^{-1}$ .

Fig. 8. Dye-traced fluid flow with counter-rotating crystal and crucible.

a-c =  $\rho=3$ ,  $\sigma=2$ ; d-f =  $\rho=2$ ,  $\sigma=3$ .

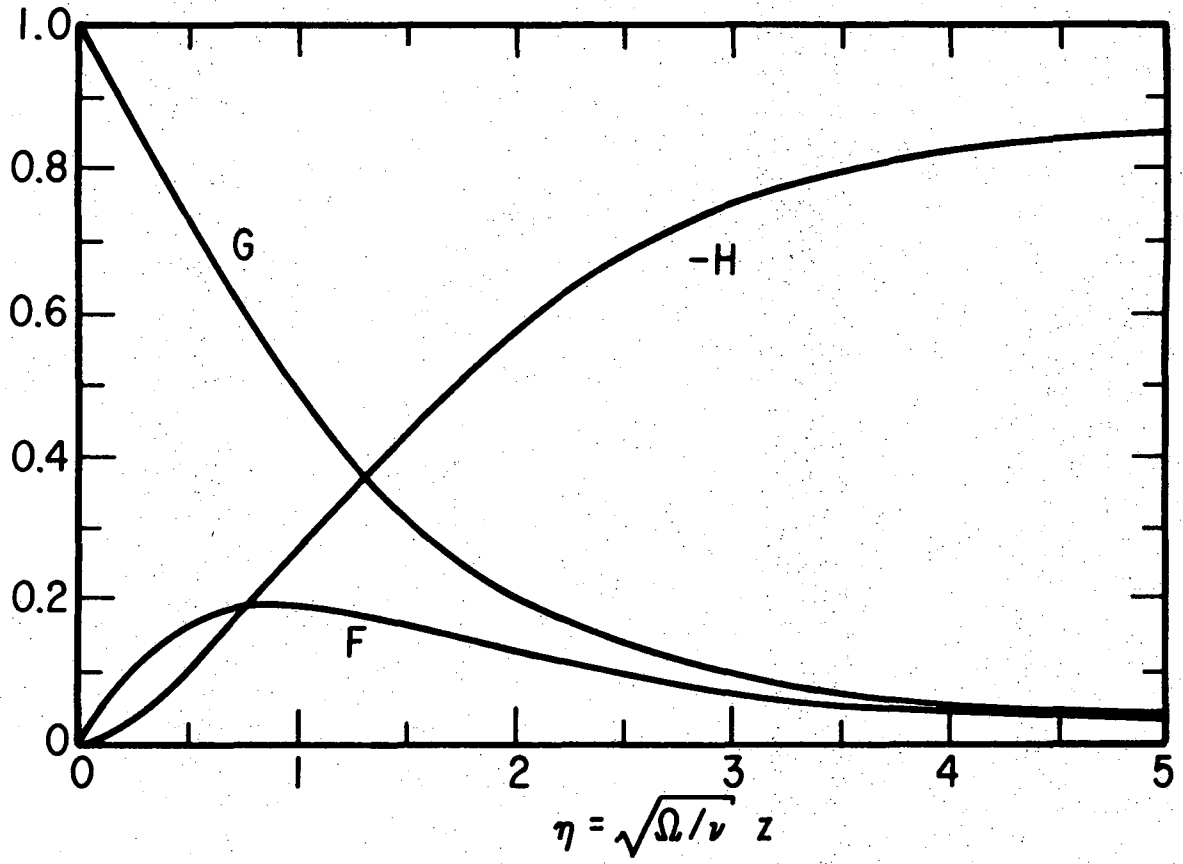
- a)  $\Omega_1 = 1.57 \text{ sec}^{-1}$ ,  $\Omega_2 = -3.14 \text{ sec}^{-1}$ ; b)  $\Omega_1 = 3.14 \text{ sec}^{-1}$ ,  $\Omega_2 = -3.14 \text{ sec}^{-1}$ ;  
c)  $\Omega_1 = 6.28 \text{ sec}^{-1}$ ,  $\Omega_2 = -1.57 \text{ sec}^{-1}$ ; d)  $\Omega_1 = 3.14 \text{ sec}^{-1}$ ,  $\Omega_2 = -3.14 \text{ sec}^{-1}$ ;  
e)  $\Omega_1 = 6.28 \text{ sec}^{-1}$ ,  $\Omega_2 = -3.14 \text{ sec}^{-1}$ ; f)  $\Omega_1 = 6.28 \text{ sec}^{-1}$ ,  $\Omega_2 = -1.57 \text{ sec}^{-1}$ .

Fig. 9. Dye-traced fluid flow, simulating Czochralski crystal growth

with counter-rotating crystal and crucible.  $\rho=3$ ,  $\sigma=3$ .

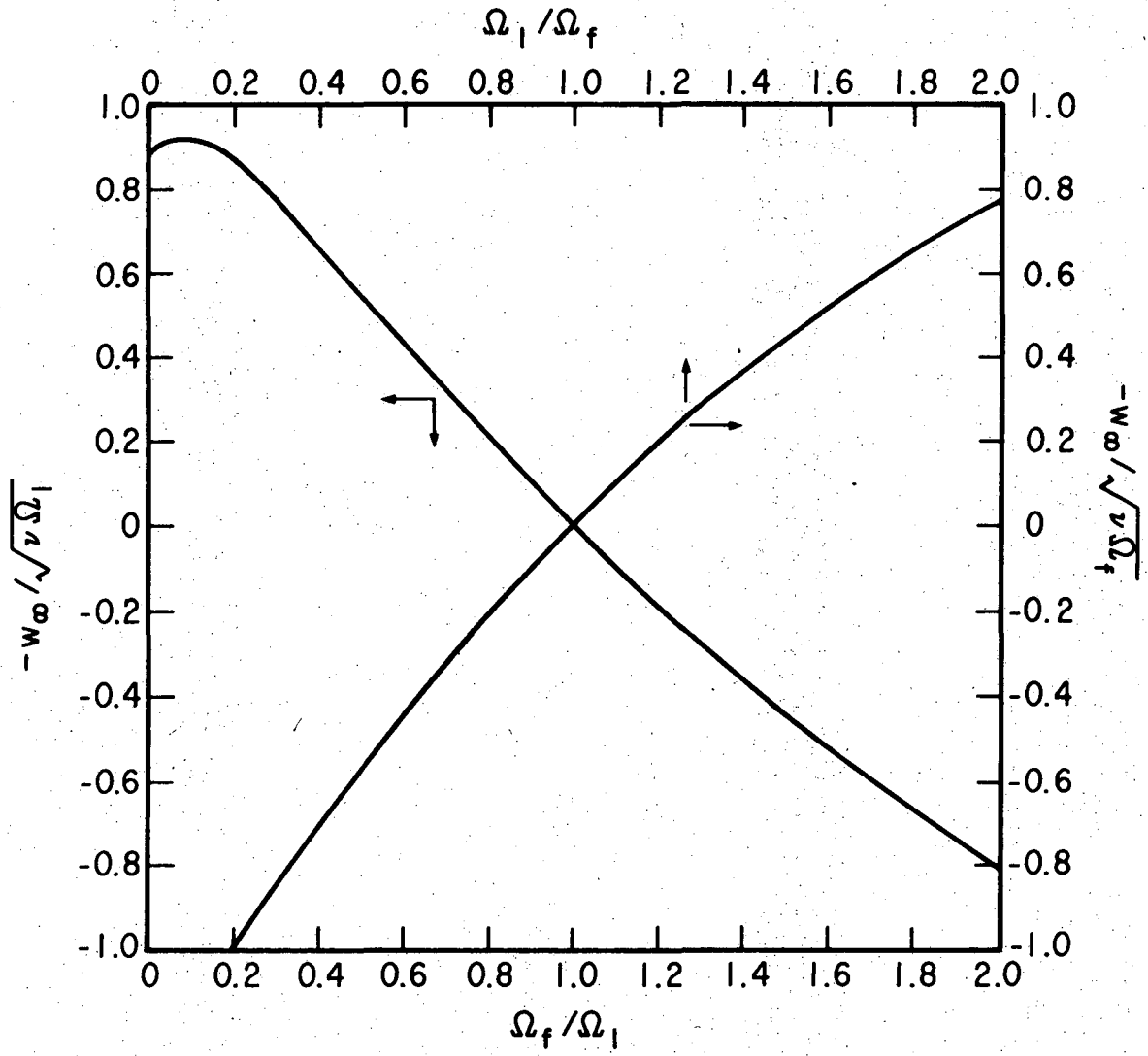
- a)  $\Omega_1 = 3.14 \text{ sec}^{-1}$ ,  $\Omega_2 = -1.57 \text{ sec}^{-1}$ ; b)  $\Omega_1 = 4.71 \text{ sec}^{-1}$ ,  $\Omega_2 = -1.57 \text{ sec}^{-1}$ ;  
c)  $\Omega_1 = 6.28 \text{ sec}^{-1}$ ,  $\Omega_2 = -1.57 \text{ sec}^{-1}$ ; d)  $\Omega_1 = 1.57 \text{ sec}^{-1}$ ,  $\Omega_2 = -3.14 \text{ sec}^{-1}$ ;  
e)  $\Omega_1 = 4.71 \text{ sec}^{-1}$ ,  $\Omega_2 = -3.14 \text{ sec}^{-1}$ ; f)  $\Omega_1 = 9.42 \text{ sec}^{-1}$ ,  $\Omega_2 = -3.14 \text{ sec}^{-1}$ ;  
g)  $\Omega_1 = 3.14 \text{ sec}^{-1}$ ,  $\Omega_2 = -4.71 \text{ sec}^{-1}$ ; h)  $\Omega_1 = 6.28 \text{ sec}^{-1}$ ,  $\Omega_2 = -4.71 \text{ sec}^{-1}$ ;  
i)  $\Omega_1 = 7.85 \text{ sec}^{-1}$ ,  $\Omega_2 = -4.71 \text{ sec}^{-1}$ .

Fig. 10. Comparison between shear layer model and experimental flow patterns.



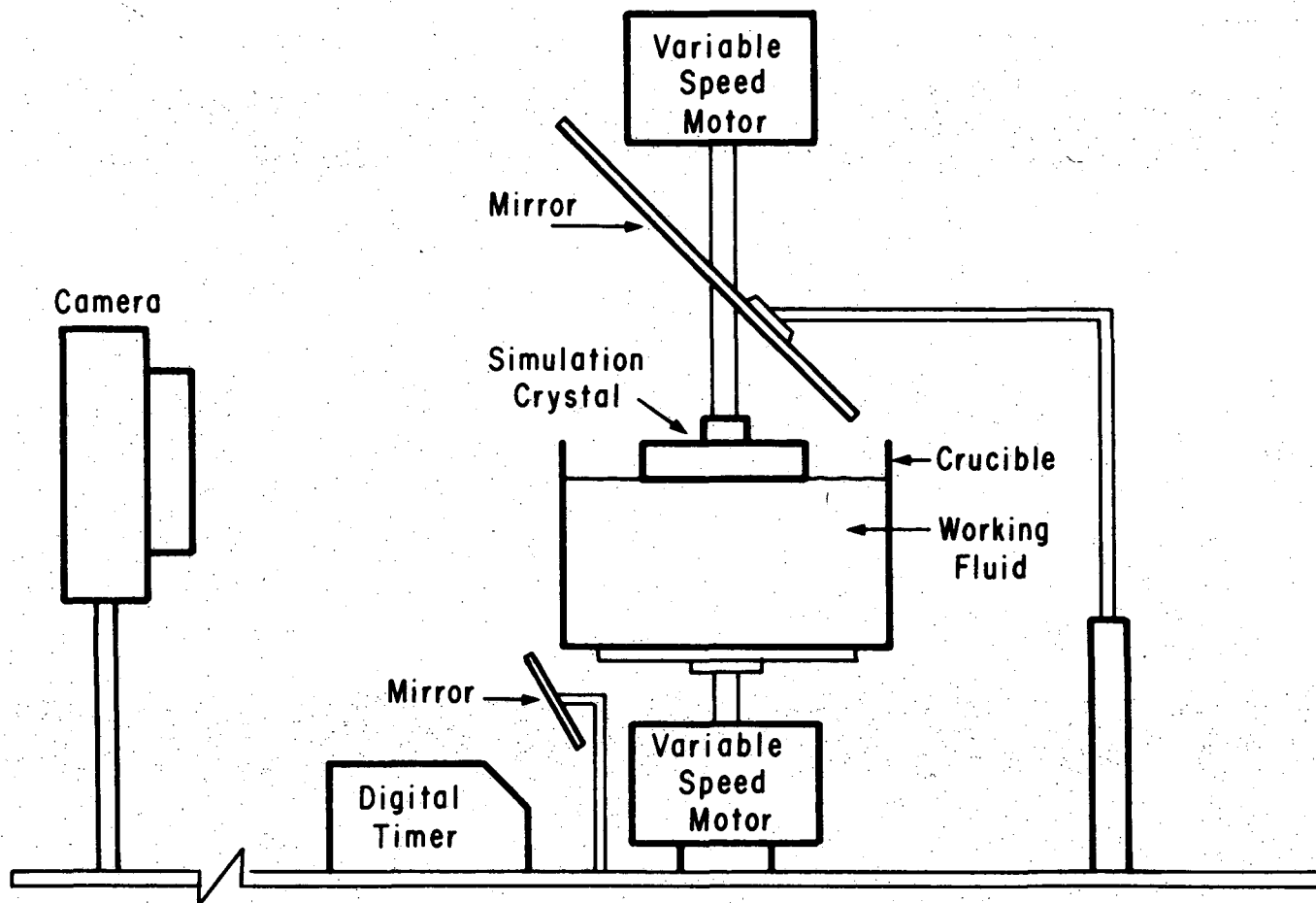
XBL 746-6577

Fig. 1.



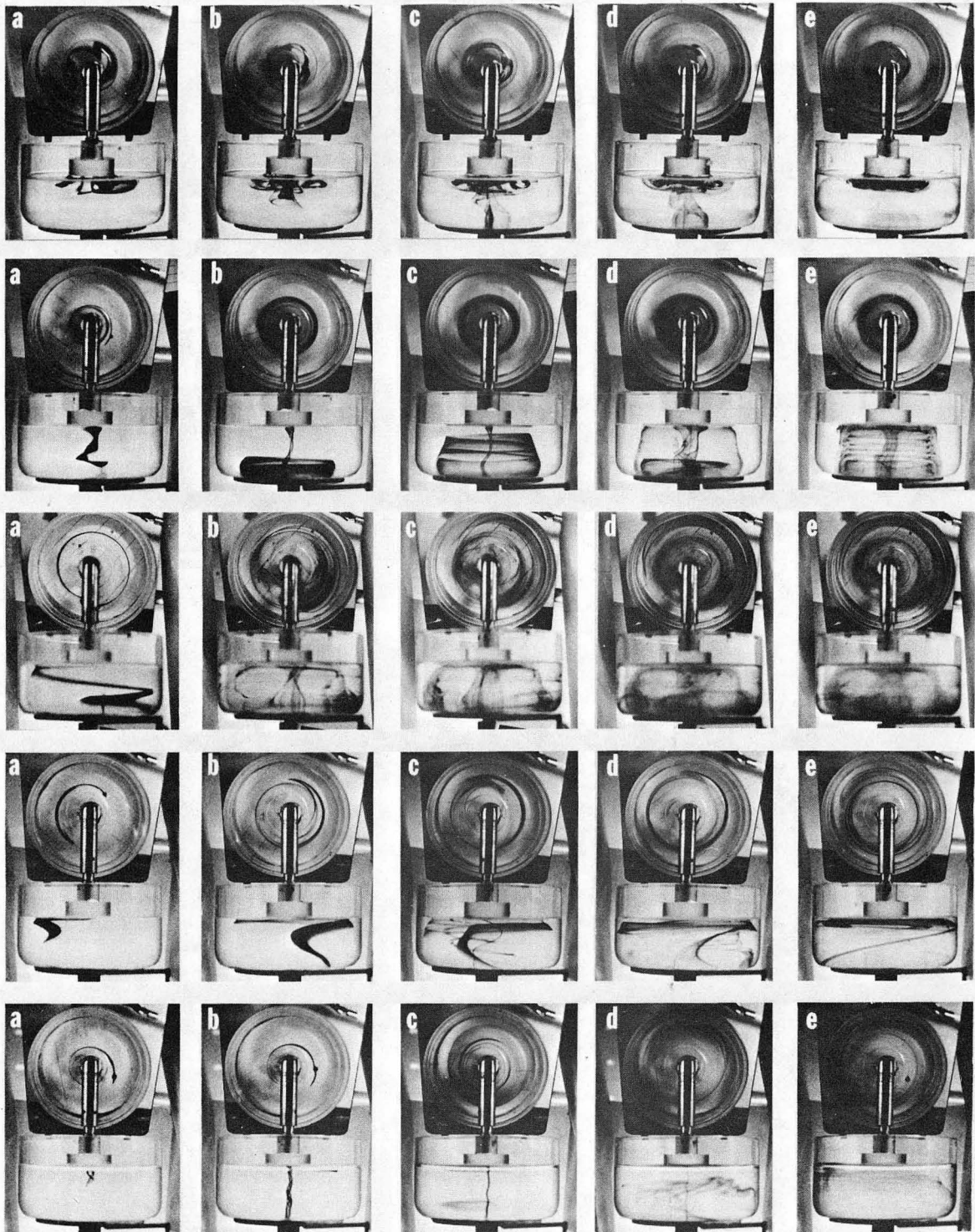
XBL 746-6567

Fig. 2.



XBL 746-6565

Fig. 3.



XBB 748-5462

Fig. 4.

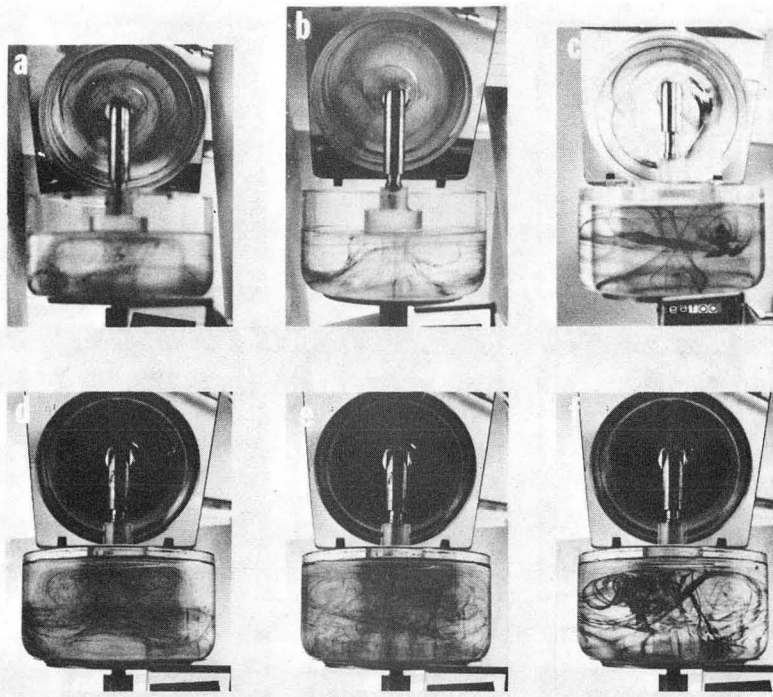
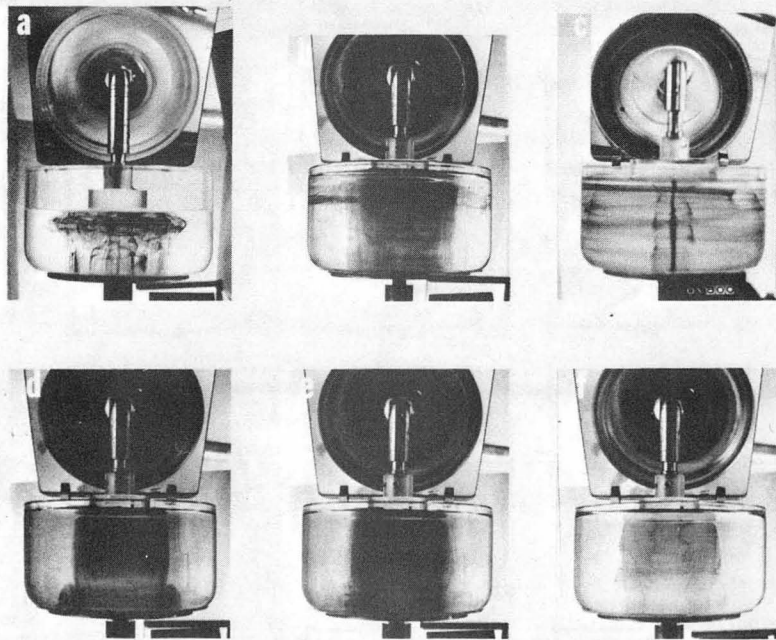


Fig. 5.



XBB 749-6060

Fig. 6.

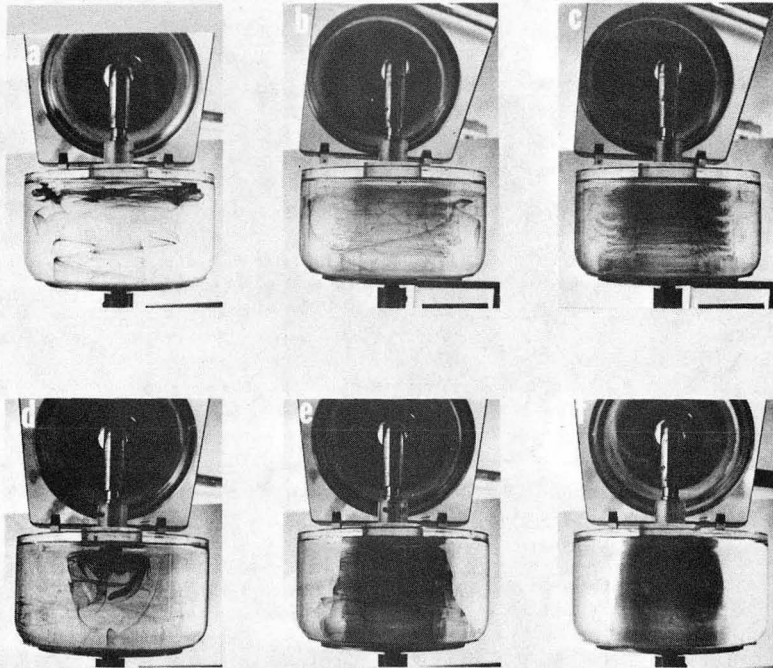
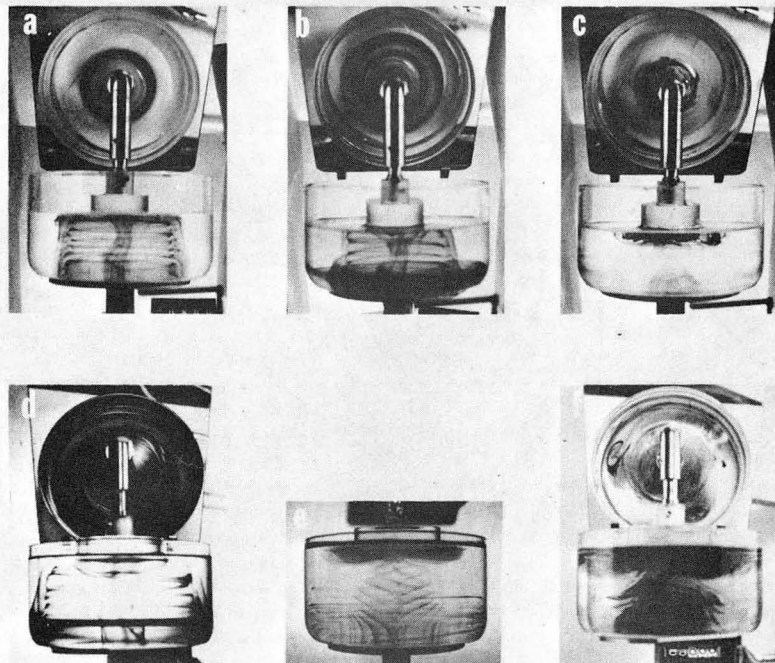
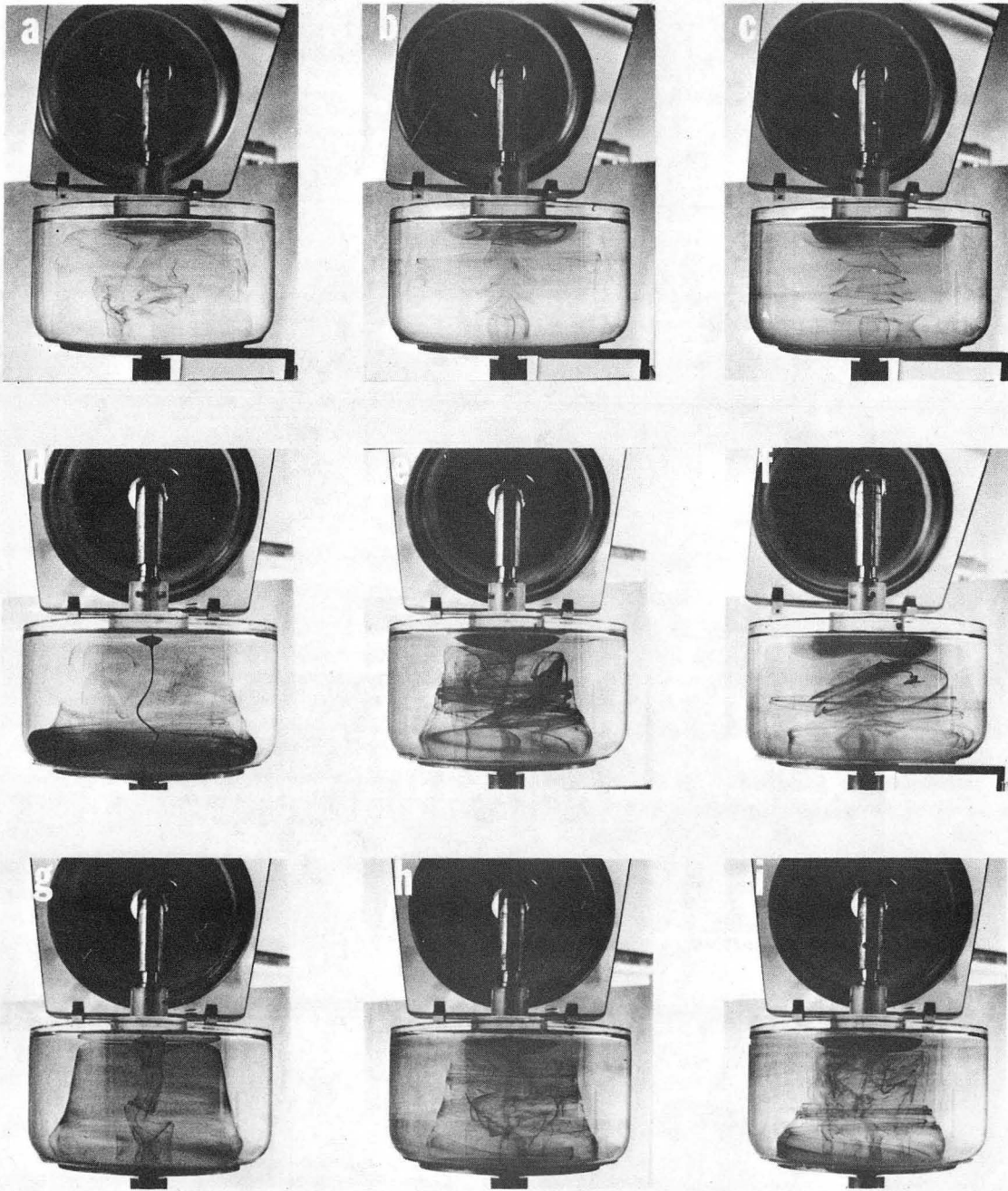


Fig. 7.



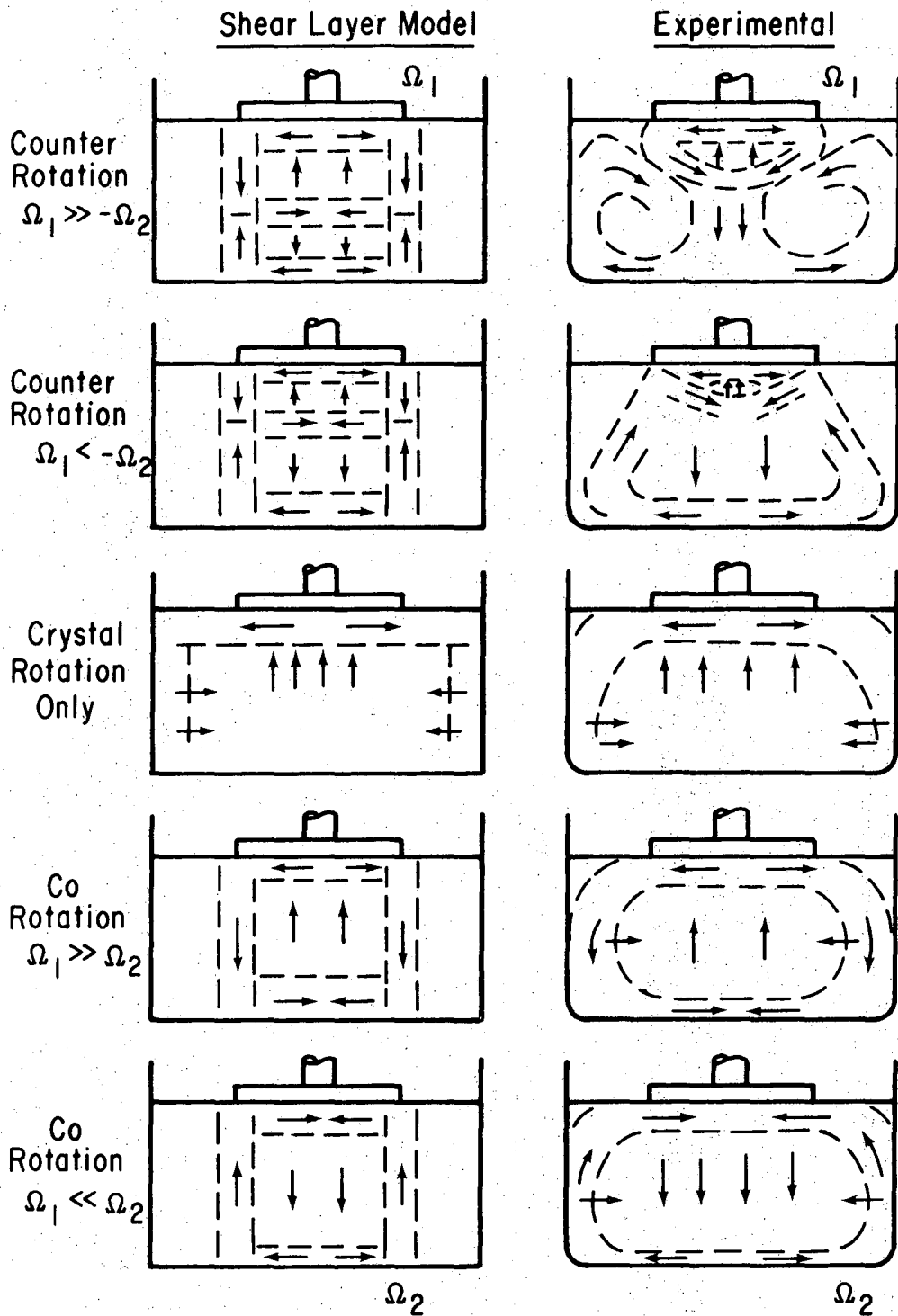
XBB 749-6059

Fig. 8.



XBB 749-6058

Fig. 9.



XBL 746-6573

Fig. 10.

REFERENCES

1. J. A. Burton, E. D. Kolb, W. P. Slichter and J. D. Struthers, J. Chem. Phys. 21, 1991 (1953).
2. A. Muller and M. Wilhelm, Z. Naturforsch. 19a, 254 (1964).
3. G. V. Komarov and A. R. Regel, Soviet Phys. - Solid State 5, 563 (1963).
4. W. D. Edwards, Can. J. Phys. 38, 439 (1960).
5. A. C. English, J. Appl. Phys. 31, 1498 (1960).
6. K. Morizane, A. F. Witt and H. C. Gatos, J. Electrochem. Soc. 114, 738 (1967).
7. K. E. Benson, Electrochem. Technol., 3, 332 (1965).
8. E. O. Schulz-DuBois, J. Crystal Growth 12, 81 (1972).
9. D. T. Hurle, J. Crystal Growth 13/14, 39 (1972).
10. H. J. Scheel and O. Schultz-DuBois, J. Crystal Growth 8, 304 (1971).
11. W. F. Merz Kirch, Int. Sci. and Technol. p.46, (October, 1966).
12. R. Eichborn, J. Heat Transfer 83, 379 (1961).
13. N. Ibl and R. H. Muller, J. Electrochem. Soc. 105, 346 (1958).
14. E. R. Pike, D. A. Jackson, P. J. Bourke and D. I. Page, J. Sci. Instr. 2, 727 (1968).
15. A. J. Goss and R. E. Arlington, Marconi Rev. 22, 132 (1959).
16. B. M. Turouskii and M. G. Mil'vidskii, Soviet Phys. - Cryst. 6, 606 (1962).
17. D. S. Robertson, Brit. J. Appl. Phys. 17, 1047 (1966).
18. J. R. Carruthers, J. Electrochem. Soc. 114, 959 (1967).
19. J. R. Carruthers and K. Nassau, J. Appl. Phys. 39, 5205 (1968).

20. G. I. Taylor, Phil. Trans. Roy. Soc. (London) A, 223, 289 (1923).
21. S. Chandrasekhas, "Hydrodynamic and Hydrodynamic Stability," Oxford University Press, London, 1961, p. 66.
22. G. K. Batchelor, Quart. J. Mech. Appl. Math. 4, 29 (1951).
23. G. N. Lance and M. H. Rogers, Proc. Roy. Soc. A 266, 109 (1962).
24. C. E. Pearson, J. Fluid Mech. 21, 623 (1965).
25. C. J. Stephenson, J. Fluid Mech 38, 335 (1969).
26. F. Schulz-Grunow, Z. angew. Mech. 15, 191 (1935).
27. K. G. Picha and E. R. G. Eckert, Proc. 3rd U.S. Nat'l Cong. on Appl. Mech., pp 791-798 (1958).
28. K. Stewartson, Proc. Cambridge Phil. Soc. 49, 333 (1953).

### III. SOLVENT SELECTION FOR CONGRUENT SATURATION OF MAGNETIC GARNETS

#### A. Introduction

Liquid phase epitaxy (L.P.E.) has been used as a means of depositing homoepitaxial<sup>1</sup> and heteroepitaxial<sup>2</sup> thin film for magnetic bubble domain devices. A large quantity of research has been performed showing that bubble domain memory devices fabricated from these materials have the capability to operate at high speeds with significantly low data access times.<sup>3,4</sup> The magnetic bubble domain device is a powerful product for computer architects. Compared with other technologies in the storage field such as drums, disks and tapes, bubble technology has the advantage of nonvolatility and nondestructive readout.<sup>5</sup> Work is now concentrated on the magnetic garnet films. These materials can support bubble domains with diameters between 1 and 15  $\mu\text{m}$ , with 5  $\mu\text{m}$  diameter bubbles widely used in working devices.<sup>6</sup> In the L.P.E. technique a supersaturated solution of rare earth oxides and ferric oxide is prepared in some proper solvents, and brought into contact with a non-magnetic substrate such as gadolinium gallium garnet (GGG), where solution crystal growth occurs. To ensure that the films grown are uniform in composition and thickness, the substrate are given an axial rotation.

There are two major solvents presently used for L.P.E. growth of the bubble garnets, the lead oxide-base flux and the barium oxide-base flux. Each of them has its own advantages and disadvantages with regard to volatility, reactivity with the platinum crucible, solubility

of magnetic garnets and solvent incorporation.<sup>7</sup> At present the PbO-base flux is still used most widely on the industrial scale because of low viscosity and low growth temperature. Several solvent systems have been studied for garnet crystal growth. These are (a) PbO-PbF<sub>2</sub>, (b) PbO-B<sub>2</sub>O<sub>3</sub>-PbF<sub>2</sub>, (c) PbO-B<sub>2</sub>O<sub>3</sub> and (d) BaO-B<sub>2</sub>O<sub>3</sub>-BaF<sub>2</sub>. Conventionally, solvents (a) and (b) are used to grow bulk garnet crystal.<sup>10-12</sup> Both of these solvents present some disadvantages in that growth of iron garnets requires higher temperature (~ 1300°C), the weight loss of solvent is high, and the density of solvent inclusions is high.<sup>9</sup> For the solvent PbO, the addition of 2 weight % B<sub>2</sub>O<sub>3</sub> suppresses the precipitation of the magnetoplumbite phase. The solvent BaO-B<sub>2</sub>O<sub>3</sub>-BaF<sub>2</sub> is quite new and is advantageous in several respects.<sup>7</sup> The advantages of BaO-B<sub>2</sub>O<sub>3</sub> base solvents over PbO-base fluxes are reduced solvent evaporation, lower corrosion of platinum crucible, less solvent incorporation in the garnets during crystal growth and higher solubility of garnet oxides. The viscosity of the BaO-B<sub>2</sub>O<sub>3</sub>-base solvents is, however, much higher than that of the PbO-base solvents.

The composition and temperature range for precipitation of the desired phase from a given solvent is often severely limited. Often, the composition change of the solution during crystal growth is unknown, and replenishment of the garnet phase components for solvent re-use is not an easy matter. Hence, the solution remaining after solution growth is normally discarded. This is economically an impractical procedure.

If a solvent could be found which allows congruent saturation of the garnet phase, then regeneration of the solvent would be possible, and the yield and economy of the LPE process could be improved.

### B. Phase Equilibria

The solutions required for LPE growth of magnetic garnet films are complicated multicomponent systems which contain rare earth oxides, iron and non-magnetic oxides of tri-valent ions, and solvent components. Table I summarizes the current literature on LPE growth of garnet films from PbO-based, and BaO-based solvents. The compositions of the garnet compounds are presented along with the solvent compositions, initial molar ratios of garnet oxides to solvent oxides, and growth temperatures.

Because the rare earths occupy the dodecahedral sites in the garnet lattice, while tri-valent iron and smaller ions occupy the tetrahedral and dodecahedral sites, it is convenient to represent the multicomponent solution in a pseudo-ternary phase diagram with the relatively insoluble solvent oxides taken as the first component, the oxides of the dodecahedral ions taken as the second, and oxides of the tetrahedral and octahedral ions taken as the third.

The pseudo-ternary representation of the initial solution compositions for LPE growth of magnetic garnets is shown in Fig. 1.

Figure 2 shows an expanded section of the pseudo-ternary phase field showing the initial solution compositions for LPE growth of the garnet phase. The PbO-PbF<sub>2</sub> solvents allow the highest solubility, followed by PbO-PbF<sub>2</sub>-B<sub>2</sub>O<sub>3</sub>, BaO-BaF<sub>2</sub>-B<sub>2</sub>O<sub>3</sub> and PbO-B<sub>2</sub>O<sub>3</sub> solvents in

order of decreasing solubility of the garnet phase. The garnet-solvent pseudo-binary tie line separates the ternary phase field into two regions. All of the solutions containing PbO-base solvents appear above the tie line and require an excess of iron oxide in the melt for equilibrium with the garnet phase, while the solutions containing BaO-base solvents appear below the tie line and require an excess of the rare earth oxides for the required phase equilibrium. Mixtures of the BaO-based, and PbO-based solvents should allow congruent saturation of the garnet phase. The corresponding mixed solvent ranges are indicated in the pseudo ternary phase field of Fig. 2 by dashed lines. It is evident that mixtures of the PbO-based and BaO-based solvents should allow congruent saturation of a given garnet compound.

The experimental data summarized in Fig. 2 indicates that the garnet solubility in PbO can be modified by the addition of  $B_2O_3$  and  $PbF_2$  to the solvent. In order to preserve the congruency of saturation during precipitation of the garnet, it is also essential that the projected normal to the liquidus surface lie along the line of congruency. This condition would require a mixture of the three solvents B, C, and D shown in Fig. 2. In this study, simplified binary mixtures of solutions C and D were studied to test congruent saturation of the garnet  $EuEr_2Ga_{0.7}Fe_{4.3}O_{12}$  at a single growth temperature.

The experiment data summarized in Fig. 2 indicate that the crystal growth compositions of solutions C and D lie on opposite sides of the line of congruent saturation (shown dotted). This suggests that

some mixture of the two fluxes would yield a congruently saturating solution. This hypothetical mixture has been determined by assuming mixed solvent solutions to be ideal. This extrapolated congruently saturating solvent then contains the following mole percentages = 5.8%  $\text{Re}_2\text{O}_3$ , 9.6% ( $\text{Ga}_2\text{O}_3 + \text{Fe}_2\text{O}_3$ ), and 84.6% solvent. The ratio of garnet oxides to flux is therefore 1:5.5.

In order to crystallize  $\text{EuEr}_2\text{Ga}_{0.7}\text{Fe}_{4.3}\text{O}_{12}$ , from a congruently saturating solution, the molar composition of the component garnet oxides is fixed at 12.5%  $\text{Eu}_2\text{O}_3$ , 25%  $\text{Er}_2\text{O}_3$ , 8.75%  $\text{Ga}_2\text{O}_3$ , and 53.75%  $\text{Fe}_2\text{O}_3$ . The composition of the flux was determined from Fig. 2 using the lever rule to obtain the ratio of solvent C to solvent D, 1:2.8, where the composition for solvent C and solvent D are from Table I, 94%  $\text{PbO} + 6\% \text{B}_2\text{O}_3$  and 41%  $\text{BaO} + 18\% \text{BaF}_2 + 41\% \text{B}_2\text{O}_3$ , respectively. Since the amounts of  $\text{B}_2\text{O}_3$  in solvent C, and  $\text{BaF}_2$  in solvent D, are not predominant, the solvent system is further simplified by omitting these components. Therefore, the solvent system proposed for study of congruent saturation experiments is the system  $(\text{PbO})_x(\text{BaO} \cdot \text{B}_2\text{O}_3)_{1-x}$  and the predicted congruently saturating composition is  $x=0.26$ .

The composition of the solution for garnet crystal growth has been specified by molar ratios of component oxides,  $R_1$ . The ratios conventionally specified for liquid phase epitaxial growth are

Table. 1. Solvents and Growth Conditions for Garnet Crystal Growth

Garnet	Solvent (mole %)	Solution Composition (mole %)	Garnet oxides (mole %)	Growth Temp (°C)	Ref.
1. $\text{Eu}_{1.1}\text{Yb}_{1.9}\text{Fe}_5\text{O}_{12}$	PbO 94, $\text{B}_2\text{O}_3$ 6	$\text{Eu}_2\text{O}_3$ 0.264, $\text{Yb}_2\text{O}_3$ 0.456, $\text{Fe}_2\text{O}_3$ 9.0, PbO 84.83, $\text{B}_2\text{O}_3$ 5.45	9.71	880	8
2. $\text{EuEr}_2\text{Ga}_{0.7}\text{Fe}_{4.3}\text{O}_{12}$	PbO 89, $\text{B}_2\text{O}_3$ 11	$\text{Eu}_2\text{O}_3$ 0.303, $\text{Er}_2\text{O}_3$ 0.587, $\text{Fe}_2\text{O}_3$ 6.5, $\text{Ga}_2\text{O}_3$ 1.06, PbO 81.15, $\text{B}_2\text{O}_3$ 10.4	8.48	950-870	9
3. $\text{Yb}_2\text{Eu}_{0.5}\text{Tm}_{0.5}\text{Ga}_{0.5}\text{Fe}_{4.5}\text{O}_{12}$	PbO 94, $\text{B}_2\text{O}_3$ 6	$\text{Y}_2\text{O}_3$ 0.52, $\text{Eu}_2\text{O}_3$ 0.14, $\text{Tm}_2\text{O}_3$ 0.12, $\text{Fe}_2\text{O}_3$ 8.12, $\text{Ga}_2\text{O}_3$ 0.8, PbO 84.9, $\text{B}_2\text{O}_3$ 5.4	9.71	960	13
4. $\text{Eu}_1\text{Er}_2\text{Ga}_{0.7}\text{Fe}_{4.3}\text{O}_{12}$	PbO 94, $\text{B}_2\text{O}_3$ 6	$\text{Eu}_2\text{O}_3$ 0.58, $\text{Er}_2\text{O}_3$ 1.14, $\text{Ga}_2\text{O}_3$ 0.49, $\text{Fe}_2\text{O}_3$ 6, PbO 86.3, $\text{B}_2\text{O}_3$ 5.49	8.20	1050-850	14
5. $\text{Eu}_1\text{Er}_2\text{Ga}_{0.7}\text{Fe}_{4.3}\text{O}_{12}$	PbO 94, $\text{B}_2\text{O}_3$ 6	$\text{Eu}_2\text{O}_3$ 0.24, $\text{Er}_2\text{O}_3$ 0.48, $\text{Ga}_2\text{O}_3$ 0.5, $\text{Fe}_2\text{O}_3$ 8.46, PbO 84.87, $\text{B}_2\text{O}_3$ 5.45	9.71	970-890	15
6. $\text{Y}_3\text{Ga}_{0.57}\text{Fe}_{4.43}\text{O}_{12}$	PbO 50, $\text{PbF}_2$ 50	$\text{Y}_2\text{O}_3$ 10.20, $\text{Ga}_2\text{O}_3$ 1.76, $\text{Fe}_2\text{O}_3$ 22.9, PbO 32.5, $\text{PbF}_2$ 32.5	34.50	1265-1051	11
7. $\text{Y}_3\text{Fe}_5\text{O}_{12}$	PbO 53.3, $\text{B}_2\text{O}_3$ 7.7, $\text{PbF}_2$ 39	$\text{Y}_2\text{O}_3$ 10.0, $\text{Fe}_2\text{O}_3$ 20.0, PbO 37.3, $\text{B}_2\text{O}_3$ 5.4, $\text{PbF}_2$ 27.3	30.33	1300-950	10
8. $\text{Eu}_{0.09}\text{Gd}_{2.32}\text{Tb}_{0.59}\text{Fe}_5\text{O}_{12}$	PbO 43.7, $\text{B}_2\text{O}_3$ 7.7, $\text{PbF}_2$ 48.6	$\text{Eu}_2\text{O}_3$ 0.2, $\text{Gd}_2\text{O}_3$ 5.1, $\text{Tb}_2\text{O}_3$ 1.3, $\text{Fe}_2\text{O}_3$ 19.9, PbO 32.1, $\text{B}_2\text{O}_3$ 5.7, $\text{PbF}_2$ 35.7	26.33	1300-950	12
9. $\text{Er}_2\text{Tb}_1\text{Al}_{1.1}\text{Fe}_3.9\text{O}_{12}$	PbO 43.6, $\text{B}_2\text{O}_3$ 7.8, $\text{PbF}_2$ 48.6	$\text{Eu}_2\text{O}_3$ 6.5, $\text{Tb}_2\text{O}_3$ 3.4, $\text{Al}_2\text{O}_3$ 4.4, $\text{Fe}_2\text{O}_3$ 15.5, PbO 30.6, $\text{B}_2\text{O}_3$ 5.5, $\text{PbF}_2$ 34.1	29.40	1300-950	12
10. $\text{Eu}_1\text{Er}_2\text{Ga}_{0.7}\text{Fe}_{4.3}\text{O}_{12}$	BaO 40.9, $\text{B}_2\text{O}_3$ 41.3, $\text{BaF}_2$ 17.8	$\text{Eu}_2\text{O}_3$ 2.7, $\text{Er}_2\text{O}_3$ 5.5, $\text{Ga}_2\text{O}_3$ 1.5, $\text{Fe}_2\text{O}_3$ 9.4, BaO 33.1, $\text{B}_2\text{O}_3$ 33.4, $\text{BaF}_2$ 14.4	19.22	1000	7
11. $\text{Gd}_{0.7}\text{Y}_{1.55}\text{Yb}_{0.75}\text{Ga}_{0.9}\text{Fe}_{4.1}\text{O}_{12}$	BaO 40.3, $\text{B}_2\text{O}_3$ 4.15, $\text{BaF}_2$ 18.2	$\text{Gd}_2\text{O}_3$ 1.9, $\text{Y}_2\text{O}_3$ 4.1, $\text{Yb}_2\text{O}_3$ 2.3, $\text{Ga}_2\text{O}_3$ 2.3, $\text{Fe}_2\text{O}_3$ 9.4, BaO 32.2, $\text{B}_2\text{O}_3$ 33.2, $\text{BaF}_2$ 14.6	20.00	1140-990	7

$$\frac{\text{Fe}_2\text{O}_3}{\Sigma \text{Ln}_2\text{O}_3} = R_1$$

$$\frac{\text{Fe}_2\text{O}_3}{\text{Ga}_2\text{O}_3} = R_2$$

$$\frac{\text{PbO}}{\text{BaO}} = R_3$$

$$\frac{\Sigma \text{Ln}_2\text{O}_3 + \text{Fe}_2\text{O}_3 + \text{Ga}_2\text{O}_3}{\Sigma \text{Ln}_2\text{O}_3 + \text{Fe}_2\text{O}_3 + \text{Ga}_2\text{O}_3 + \text{B}_2\text{O}_3 + \text{BaO} + \text{PbO}} = R_4$$

where Ln is a rare earth metal.

According to the arguments above, the molar ratios predicted for congruent saturation of the garnet phase in the solvent are then

$$R_1 = 1.43$$

$$R_2 = 6.14$$

$$R_3 = 0.7$$

$$R_4 = 0.154$$

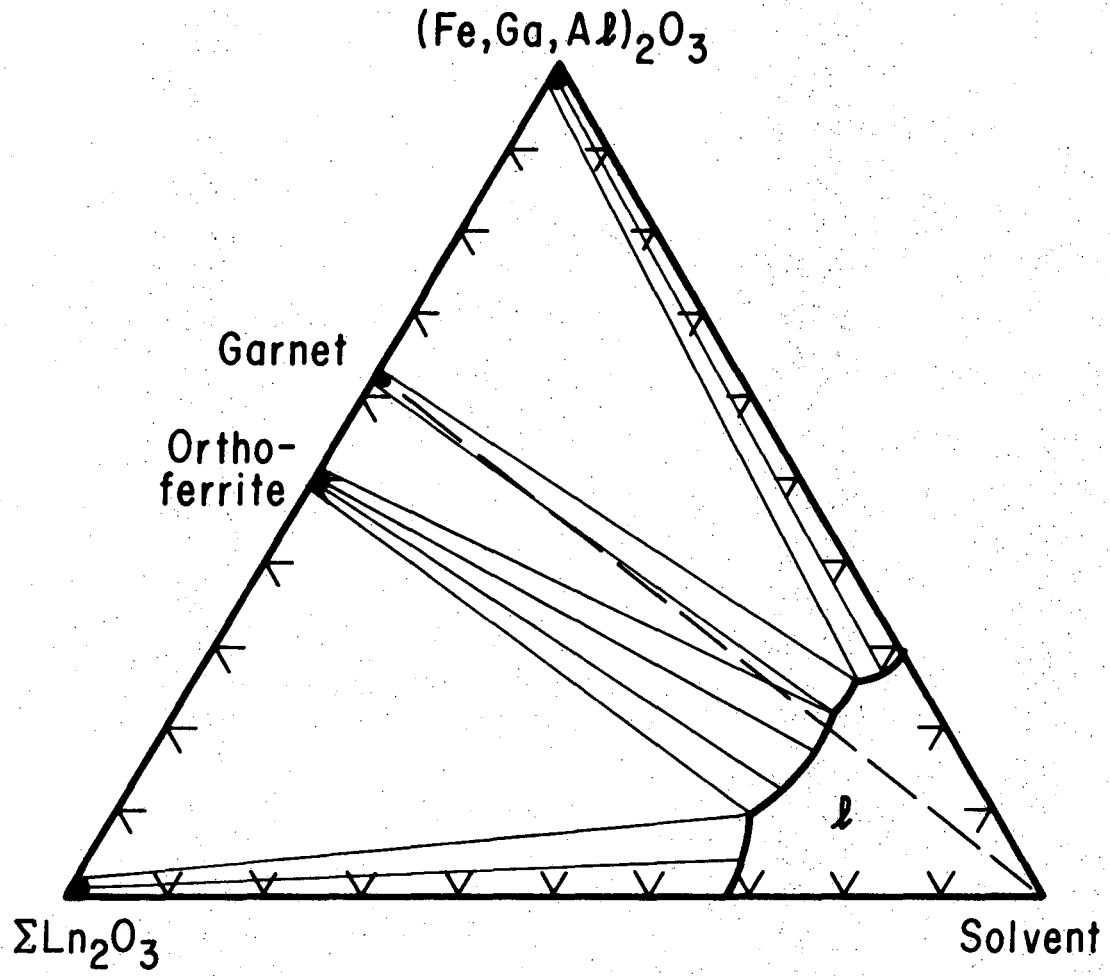
The required value of  $R_4$  is somewhat dependent on the composition of the garnet films.

FIGURE CAPTIONS

Fig. 1. Isothermal section of the simplified ternary phase diagram for garnet growth.

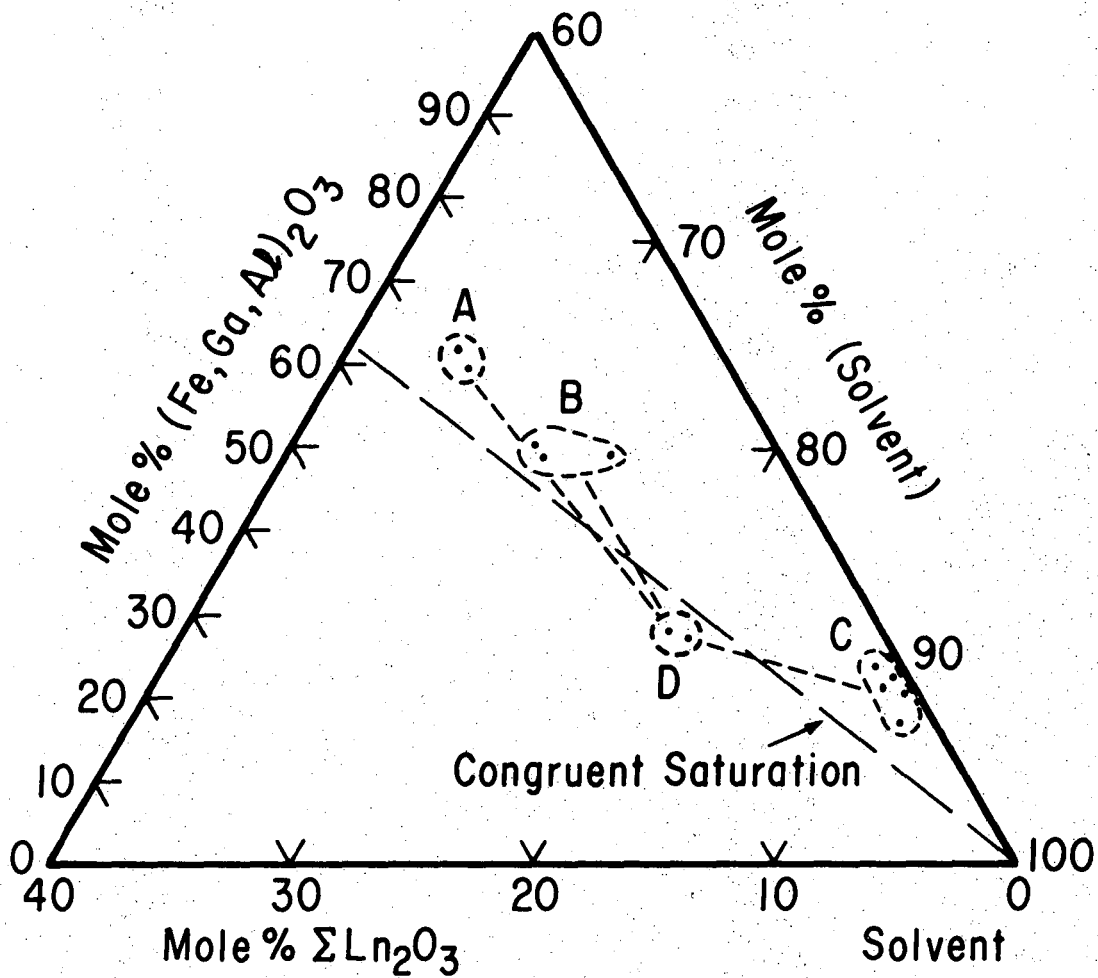
Fig. 2. Solvent-rich corner of the simplified ternary phase diagram showing solution compositions for garnet growth from

A)  $\text{PbO-PbF}_2$ , B)  $\text{PbO-PbF}_2\text{-B}_2\text{O}_3$ , C)  $\text{PbO-B}_2\text{O}_3$  and D)  $\text{BaO-BaF}_2\text{-B}_2\text{O}_3$  solvents.



XBL 746-6561

Fig. 1.



XBL 746-6560

Fig. 2.

REFERENCES

1. J. M. Robertson, M. J. G. Van Hout, M. M. Janssen and W. T. Stacy, J. Crystal Growth 18, 294 (1973).
2. R. C. Linares, J. Crystal Growth 4, 443 (1968).
3. G. S. Almasi, et.al., Proc. Am. Inst. Phys. 5, 220 (1971).
4. A. H. Bobeck and H. D. E. Scovil, Scientific American 224, 78, (1971).
5. W. C. Marity and J. P. Davis, Wescon Technical paper session 8 (Sept. 1972).
6. A. H. Bobeck, IEEE Trans. on Magnetics Mag-6, 445 (1970).
7. R. Hiskes, T. L. Felonler and R. A. Burmeister, J. Elect. Mat. 1, 458 (1972).
8. R. Ghez and E. A. Gress, Mat. Res. Bull. 8, 31 (1973).
9. H. H. Quon and A. J. Potrin, Mat. Res. Bull. 7, 463 (1972).
10. W. H. Grodkiewicz, E. F. Dearborn and L. G. Van Uitert, in Crystal Growth, H. S. Peiser, ed., Pergamon Press, Oxford 1967, p. 441.
11. J. W. Nielson, D. A. Lepore and D. C. Leo, *ibid*, p. 457.
12. L. G. Van Uitert, W. A. Bonner, W. H. Grodkiewicz, L. Pictroski and G. J. Zydzik, 5, 825 (1970).
13. W. A. Bonner, J. E. Geusic, D. H. Smith, L. G. Van Uitert and G-P. Vella-Coleiro, Mat. Res. Bull. 8, 785 (1973).
14. L. K. Shick, J. W. Nielsen, A. B. Bobeck, A. J. Kentzig, P. C. Michaels and J. P. Reekstin, Appl. Phys. Letters 18, 89 (1971).
15. H. J. Levinstein et.al., Appl. Phys. Letters, 19, 486 (1971).

IV. AN EXPERIMENTAL STUDY OF THE PbO-BaO·B<sub>2</sub>O<sub>3</sub> SOLVENT SYSTEM FOR  
CONGRUENT SATURATION AND LIQUID PHASE EPITAXIAL GROWTH OF  
EuEr<sub>2</sub>Fe<sub>4.3</sub>Ga<sub>0.7</sub>O<sub>12</sub> FILMS

A. Introduction

Mixed solvents in the PbF<sub>2</sub>-PbO-BaO-BaF<sub>2</sub>-B<sub>2</sub>O<sub>3</sub> system offer potential for congruent saturation of rare-earth substituted garnets in liquid phase epitaxial growth processes. Congruent saturation of the garnet phase has the property that components of the garnet phase have the same ratio in the solution-grown film as in the solution. As a consequence, the yield of liquid phase epitaxially grown films is potentially great, without the deposition of undesired phases.

Conditions for garnet phase growth from solution with different solvents are exemplified for rare-earth iron garnets whose phase diagram are shown in Fig. 1. With a PbO solvent the solution composition range for garnet-liquid phase equilibrium is limited to a narrow range at a given isotherm, as shown in Fig. 1a. A large excess of Fe<sub>2</sub>O<sub>3</sub> is required, and the rare-earth component is easily depleted from the crystallization interface during deposition. A solvent which causes displacement of the range of garnet-liquid phase equilibrium toward the rare-earth corner of the ternary triangle is shown in Fig. 1b. For this solvent the garnet phase is congruently saturated at point a, but solution growth causes a displacement from the line of congruency. For the solvent of Fig. 1c, the garnet phase is again congruently saturated at point a and congruency is maintained during solution growth.

In this study, the binary solvent system  $\text{PbO-BaO}\cdot\text{B}_2\text{O}_3$  was explored with regard to phase equilibria and growth characteristics of  $\text{EuEr}_2\text{Fe}_{4.3}\text{Ga}_{0.7}\text{O}_{12}$  films. An evaluation of phase equilibria for garnet solubilities in  $\text{PbO-PbF}_2$ ,  $\text{PbO-PbF}_2\text{-B}_2\text{O}_3$ ,  $\text{PbO-B}_2\text{O}_3$  and  $\text{BaO-BaF}_2\text{-B}_2\text{O}_3$  solvent systems indicates that  $\text{EuEr}_2\text{Fe}_{4.3}\text{Ga}_{0.7}\text{O}_{12}$  should congruently saturate a solvent containing 26 mole%  $\text{PbO}$ , 37 mole%  $\text{BaO}$  and 37 mole%  $\text{B}_2\text{O}_3$ . Under conditions of congruent saturation, the component mole fractions in the solvent are present in the same ratios as in the garnet phase.

Consider a solution for liquid phase epitaxial growth containing 5.8 mole% rare earth oxides with  $\text{Eu}_2\text{O}_3$  and  $\text{Er}_2\text{O}_3$  present in the ratio of 1:2, 9.6 mole% group III element oxides (nonrare-earths  $\text{Fe}$ ,  $\text{Ga}$ , etc.) with  $\text{Fe}_2\text{O}_3$  and  $\text{Ga}_2\text{O}_3$  present in the ratio of 6:1, and 84.6 mole% solvent consisting of 26 mole%  $\text{PbO}$  and 74 mole%  $\text{BaO}\cdot\text{B}_2\text{O}_3$ . The corresponding molar ratios are then given by:

$$R_1 = \frac{\text{Fe}_2\text{O}_3}{\Sigma \text{Ln}_2\text{O}_3} = 1.43$$

$$R_2 = \frac{\text{Fe}_2\text{O}_3}{\text{Ga}_2\text{O}_3} = 6.14$$

$$R_3 = \frac{\text{PbO}}{\text{BaO}} = 0.7$$

$$R_4 = \frac{\Sigma \text{Ln}_2\text{O}_3 + \text{Fe}_2\text{O}_3 + \text{Ga}_2\text{O}_3}{\Sigma \text{Ln}_2\text{O}_3 + \text{Fe}_2\text{O}_3 + \text{Ga}_2\text{O}_3 + \text{BaO} + \text{B}_2\text{O}_3 + \text{PbO}} = 0.154$$

These ratios for the  $\text{PbO}\cdot\text{BaO}\cdot\text{B}_2\text{O}_3$  mixed solvent are considerably different from those given by Blank<sup>1</sup> for the 98 mole%  $\text{PbO}$  + 2 mole%  $\text{B}_2\text{O}_3$  solvent for which

$$R_1 = 14,$$

$$R_2 = 16,$$

$$R_3 = \frac{\text{PbO}}{\text{B}_2\text{O}_3} = 15.6$$

$$R_4 = 8.45$$

because non-stoichiometric ratios of the garnet phase components are required in the  $\text{PbO}$ -base solvent.

To test for congruency of saturation of the garnet phase, solvents containing 18, 26 and 34 mole%  $\text{PbO}$  in  $\text{BaO}\cdot\text{B}_2\text{O}_3$  were chosen for study. These solvent compositions are shown in Fig. 2 and compared with other solvents from which yttrium-iron garnet (YIG) is known to crystallize. It can be seen that the three solvent compositions lie within the phase field for crystallization of YIG.

In order to test for congruency of garnet saturation in solutions containing different mole fractions of garnet oxide, solvents with different composition parameters  $R_4$  were chosen. In addition to the value  $R_4 = 0.154$  (garnet oxides/solvent = 1/5.5), predicted from simple solubility theory the values  $R_4 = 0.10$  (garnet oxides/solvent = 1/9) and  $R_4 = 0.20$  (garnet oxides/solvent = 1/4) were chosen. These nine solution compositions are summarized in Table 1.

Table 1. Solution Compositions for Garnet Film Growth

Sample #	<u>garnet oxides</u> <u>solvent</u> (molar ratio)	<u>Flux Composition (mole%)</u>	
		PbO	BaO·B <sub>2</sub> O <sub>3</sub>
1	1 : 5.5	26	74
2	1 : 5.5	18	82
3	1 : 5.5	34	66
4	1 : 9	26	74
5	1 : 9	18	82
6	1 : 9	34	66
7	1 : 4	26	74
8	1 : 4	18	82
9	1 : 4	34	66

### B. Experimental Apparatus and Method

All the melts were prepared from high purity garnet component oxides and reagent purity solvent oxides. In each experiment 99.99% pure PbO, 99% BaO, reagent grade B<sub>2</sub>O<sub>3</sub>, 99.99% Eu<sub>2</sub>O<sub>3</sub><sup>\*\*</sup>, 99.9% Er<sub>2</sub>O<sub>3</sub><sup>\*\*</sup>, 99.999% Ga<sub>2</sub>O<sub>3</sub><sup>††</sup> and 99% Fe<sub>2</sub>O<sub>3</sub><sup>‡‡</sup> were used. The composition of the garnet oxides in each solution were prepared according to the stoichiometrical ratio in the garnet phase: Eu<sub>2</sub>O<sub>3</sub> 12.5% mole, Er<sub>2</sub>O<sub>3</sub> 25% Ga<sub>2</sub>O<sub>3</sub> 8.75% and Fe<sub>2</sub>O<sub>3</sub> 53.75%. The component oxide mole fractions and weights in all solutions employed for the growth of EuEr<sub>2</sub>Ga<sub>0.7</sub>Fe<sub>4.3</sub>O<sub>12</sub> are listed in Table 2.

The substrates were cut from a boule of Czochralski-grown, (111) - oriented gadolinium gallium garnet (GGG). Thin platelets of substrate materials were cut from the boule using a 0.015 in. diamond saw.

The use of GGG as a substrate for growth of EuEr<sub>2</sub>Ga<sub>0.7</sub>Fe<sub>4.3</sub>O<sub>12</sub> film has some advantages. The lattice constant matching of the film specifically to GGG is very close, as the lattice constants for GGG and EuEr<sub>2</sub>Ga<sub>0.7</sub>Fe<sub>4.3</sub>O<sub>12</sub> are 12.382Å and 12.385Å, respectively. Thus, there will be essentially no interfacial or misfit dislocations formed so long as the lattice mismatch between film and substrate. The resistance of GGG to dissolution is somewhat superior to other garnets.

<sup>\*\*</sup> Alfa Chemical Corp., N.Y.

<sup>††</sup> Apache

<sup>‡‡</sup> Baker

Table 2. Melt Compositions for Garnet Growth of  $\text{EuEr}_2\text{Ga}_{.7}\text{Fe}_{4.3}\text{O}_{12}$

Molar ratio of garnet oxides to solvent	Solvent Composition (mole %)			Initial Melt Composition in moles (grams)							
				153.3	69.6	223.2	356	382.6	188	160 (M-W)	
	BaO	B <sub>2</sub> O <sub>3</sub>	PbO	BaO	B <sub>2</sub> O <sub>3</sub>	PbO	Eu <sub>2</sub> O <sub>3</sub>	Er <sub>2</sub> O <sub>3</sub>	Ga <sub>2</sub> O <sub>3</sub>	Fe <sub>2</sub> O <sub>3</sub>	
1	1 : 5.5	37	37	26	0.02609 (4g)	0.02586 (1.8g)	0.01882 (4.2g)	0.565	1.230	0.212	1.107
2	1 : 5.5	41	41	18	0.03118 (4.78g)	0.03118 (2.17g)	0.01366 (3.05g)	0.607	1.322	0.228	1.189
3	1 : 5.5	33	33	34	0.02211 (3.39g)	0.02212 (1.54g)	0.02276 (5.08g)	0.534	1.163	0.200	1.047
4	1 : 9	37	37	26	0.02609 (4g)	0.02586 (1.8g)	0.01882 (4.2g)	0.346	0.752	0.129	0.677
5	1 : 9	41	41	18	0.03118 (4.78g)	0.03118 (2.17g)	0.01366 (3.05g)	0.371	0.808	0.139	0.727
6	1 : 9	33	33	34	0.02211 (3.39g)	0.02212 (1.54g)	0.02276 (5.08g)	0.327	0.711	0.122	0.640
7	1 : 4	37	37	26	(4g)	(1.8g)	(4.2g)	0.777	1.692	0.291	1.522
8	1 : 4	41	41	18	(4.78g)	(2.17g)	(3.05g)	0.835	1.817	0.313	1.635
9	1 : 4	33	33	34	(3.39g)	(1.54g)	(5.08g)	0.735	1.600	0.275	1.439

Also, high quality GGG is available from commercial suppliers.

The size of GGG substrates for L.P.E. growth were 4×4×1 (mm). These were mounted in Koldmount for polishing. The polishing procedure consisted of 4 fine grinding steps on 1/0, 2/0, 3/0, 4/0, emery grade papers, followed by lapping with 6 $\mu$  and 1 $\mu$  diamond paste, and finally a Linde A (0.3 $\mu$  Al<sub>2</sub>O<sub>3</sub>)-water slurry lap in a syntron vibrator. Since substrate defects are readily replicated by the epitaxial films, and the replicated defects generally have adverse effects on bubble properties, Carefully polished substrates are essential to successful epitaxial growth.

The apparatus employed for the growth of the epitaxial garnet films is shown in Fig. 3. A platinum crucible containing a mixture of flux and nutrient materials were placed in the center of the furnace. The temperature of the flux melt was determined with a Pt-Pt 10% Rh thermocouple placed within the crucible just above the molten solution. This thermocouple was also used as a sensor for control of the furnace temperature. A LPAC-1 SCR power controller was used in either an automatic control mode or a manual control mode. Remote automatic control was also available for programmed cooling. The gadolinium gallium garnet substrate was positioned horizontally by a platinum holder attached to a ceramic tube supported by a motor drive assembly. This assembly enabled the substrate to be moved vertically or held in a fixed position while the Al<sub>2</sub>O<sub>3</sub> tube holder and substrate were

rotated. For rotation the ceramic tube holder was connected to a drive motor and variable speed control.

In each experiment the rotating substrate was placed in the furnace at a position just above the solution. After this position was maintained for several minutes in order to attain thermal equilibrium, the substrate was inserted into the melt by rotating two support knobs into grooves on the rod holder.

Solubility curves for  $\text{EuEr}_2\text{Ga}_{0.7}\text{Fe}_{4.3}\text{O}_{12}$  in different fluxes were determined by suspending a non-rotating, polished (111) GGG substrates in solutions with different amount of garnet oxides for a period of 10 minutes. The substrates were slowly withdrawn and examined visually for a deposited film. If no film was deposited, the temperature was reduced until a film was observed. The liquidus temperature was taken as the highest temperature at which an epitaxial layer appeared on the substrate. Using this liquidus data, epitaxial garnet films were grown at approximately equal supercoolings for each of the nine solution compositions.

Films of the magnetically uniaxial rare earth garnet  $\text{EuEr}_2\text{Ga}_{0.7}\text{Fe}_{4.3}\text{O}_{12}$  were grown heteroepitaxially on {111} GGG substrates by the following procedure. Prior to the dipping of the substrate into the melt the solution was heated to about 1200°C, and held at this temperature for approximately 3 hrs in order to completely dissolve the garnet component oxides and to equilibrate the melt. The temperature of the melt was then lowered to the dipping temperature. A substrate was then gradually lowered into the furnace until it reached a position

just above the melt and allowed to reach a state of thermal equilibrium. Then the rotating substrate was inserted into the molten solution. A substrate rotation rate of 60 rpm was used in most experiments. The solutions were cooled uniformly at rates of 2 ~ 6°C/min during film growth experiments. At the completion of the growth cycle the sample was slowly withdrawn from the solution.

Usually a thin layer of flux covered the surface of the samples. When desired, this layer could be dissolved in a warm, dilute solution of  $\text{HNO}_3$ . The cleaned, deposited film were examined by optical microscopy to determine film uniformity, color and secondary phase formation.

The flux coating was allowed to remain on samples examined for the composition of each layer by electron microprobe analysis. A Materials Analysis Company Model 400 electron microprobe analyzer was used to determine the distribution of each component in different layers. The electron accelerating potential was set at 20 keV in order to excite the  $L_{\alpha}$  emission from Pb. The effective emergence angle was fixed the optimum angle of 40.29° in this instrument. A monoenergetic beam of electrons was focused onto a 1-2 $\mu$  diameter spot on the specimen, where the resulting excitation of the electrons of atoms in the material produces characteristic x-radiation which is monitored by detectors, with x-ray intensities on registered on counters, whose output is periodically printed on tape for data correction and evaluation. Detection conditions for each element analyzed are summarized in Table 3.

Table 3. Element Detection Conditions for Electron Microprobe Analysis.

Element	Characteristic x-ray line	Wavelength	Analyzing crystal	Detector
Ba	$L_{\alpha}$	2.775	PET <sup>*</sup>	FPD <sup>†</sup>
Eu	$L_{\alpha}$	2.121	LiF	SPD <sup>††</sup>
Er	$L_{\alpha}$	1.784	LiF	FPD
Ga	$K_{\alpha}$	1.341	LiF	SPD
Fe	$K_{\alpha}$	1.937	LiF	FPD
Pb	$L_{\alpha}$	1.175	LiF	FPD

\* Pentaerythritol, 002 diffracting planes.

† Flow proportional Detector (93% Argon 7% Methane, 0.00025 in. mylar window).

†† Sealed proportional Detector (Xe gas, Be window).

### C. Results

The approximate liquidus temperatures for  $\text{EuEr}_2\text{Ga}_{0.7}\text{Fe}_{4.3}\text{O}_{12}$  in various solvent systems is shown in Fig. 4. These data are compared with liquidus data for other solvents by Hiskes<sup>2</sup> and Varnerin.<sup>4</sup> From these results it is obvious that the addition of  $\text{BaO}\cdot\text{B}_2\text{O}_3$  to  $\text{PbO}$  can increase the solubility of  $\text{EuEr}_2\text{Ga}_{0.7}\text{Fe}_{4.3}\text{O}_{12}$  in  $\text{PbO}$ . Weight loss by vaporization of the solvent compositions studied were found to be less than 4% at 1200°C during a half hour period. Because the volatility of  $\text{BaO}$  is much less than that of  $\text{PbO}$ , the  $\text{BaO}$  addition should lower the activity of  $\text{PbO}$  in the mixture.

Typical growth conditions are summarized in Table 4. Deposited film were examined by optical microscopy to characterize their color, surface smoothness and phase. These characteristics are summarized in Table 5. Results of molar ratios determined by the electron microprobe analysis of film and interfacial solvent compositions are shown in Tables 6 and 7. Several of the films, samples 4, 5, and 6, were of very high quality but unfortunately were too thin ( $< 5\mu$ ) to yield reliable composition data by microprobe analysis. The procedure for calculating film composition from microprobe x-ray intensity data is given in Appendix A.

The distribution coefficients for the component oxides were deduced from the microprobe data. The distribution coefficients for each component was deduced and shown in Figs. 5, 6 and 7 as a function of solvent composition. All of the distribution coefficients  $\alpha$  are nearly unity except for  $\alpha_{\text{Ba}}$  and  $\alpha_{\text{Pb}}$ . These values are much closer to unity

Table 4. Experimental Conditions for Garnet Film Growth

Sample	Garnet oxides Solvent	$\frac{\text{PbO}}{\text{BaO} \cdot \text{B}_2\text{O}_3 - \text{PbO}}$ (molar ratio)	Cooling rate (°C/min)	Growth temperature Range (°C)	Rotation (r.p.m.)
1	1 : 5.5	26	2.0	963 ~ 800	0
2	1 : 5.5	18	1.0	925 ~ 880	0
3	1 : 5.5	34	1.5	1030 ~ 988	0
4	1 : 9	26	1.0	930 ~ 890	0
5	1 : 9	18	4.0	890 ~ 850	0
6	1 : 9	34	3.3	970 ~ 750	60
7	1 : 4	26	4.0	1030 ~ 850	60
8	1 : 4	18	3.6	1010 ~ 850	60
9	1 : 4	34	3.2	1030 ~ 800	60

Table 5. Microscopic Observations of Deposited Films.

Sample	Color	Smoothness	Phase
1	yellow green	smooth	Garnet
2	yellow green	rough	Garnet with black precipitates
3	dark yellow green	rough	Garnet with black precipitates
4	golden green	excellent, smooth	Garnet
5	golden green	very smooth	Garnet
6	golden green	excellent, smooth	Garnet
7	yellow green	rough	Garnet
8	black yellow film	rough	Garnet with black precipitates
9	dark yellow green	rough	Garnet with black precipitates black spots

Table 6. Molar ratio of elements in garnet films.

Sample	Elements						Phase Deposited
	Eu	Er	Fe	Ga	Ba	Pb	
1	1.226	1.745	0.768	4.232	0.007	0.002	Garnet
2	1.400	1.580	0.520	4.480	0.009	0.010	Garnet
3	1.130	1.830	0.750	4.250	0.010	0.030	Garnet
7	1.309	1.681	0.764	4.236	0.005	0.006	Garnet
8	1.260	1.717	1.187	3.813	0.009	0.011	Garnet coated with Ferrite
9	1.171	1.811	0.731	4.261	0.004	0.014	Garnet

Table 7. The Distribution Coefficients.

Sample	Mole fraction of garnet oxides	Mole fraction of PbO in solvent	Eu	Er	Ga	Fe	Ba	Pb
1	15.4%	26%	1.24	0.88	1.10	0.98	0.42	1.82
2		18%	1.41	0.80	0.74	1.04	0.71	1.67
3		34%	1.15	0.93	1.07	0.99	0.51	1.48
7	20%	26%	1.31	0.85	1.09	0.99	0.78	1.00
8		18%	1.27	0.87	1.70	0.89	0.65	1.81
9		34%	1.18	0.91	1.04	0.99	0.47	1.52

than are values reported for the PbO-base<sup>1</sup> and BaO-base<sup>2</sup> solvents. The optimum solvent composition in the PbO-BaO·B<sub>2</sub>O<sub>3</sub> system which yields near unity distribution coefficients for Eu, Er, Fe and Ga is approximately 42 mole% PbO. The distribution coefficient for the incorporation of Ba generally was less than unity, decreased with increasing PbO mole whereas the distribution coefficient for PbO was larger than unity.

#### D. Discussion and Conclusions

Several conclusions can be drawn from the film growth data. The garnet films grown from solutions containing 10 mole% garnet oxides were found to be less affected by the solvent composition. The highest quality garnet films were formed in the three solvent compositions containing 10 mole% garnet.

For the solutions containing 15.4 and 20 mole% garnet, only the solvent containing 26 mole% PbO in BaO·B<sub>2</sub>O<sub>3</sub> produced garnet films without second phase formation at a later stage of film growth, and without solvent inclusion.

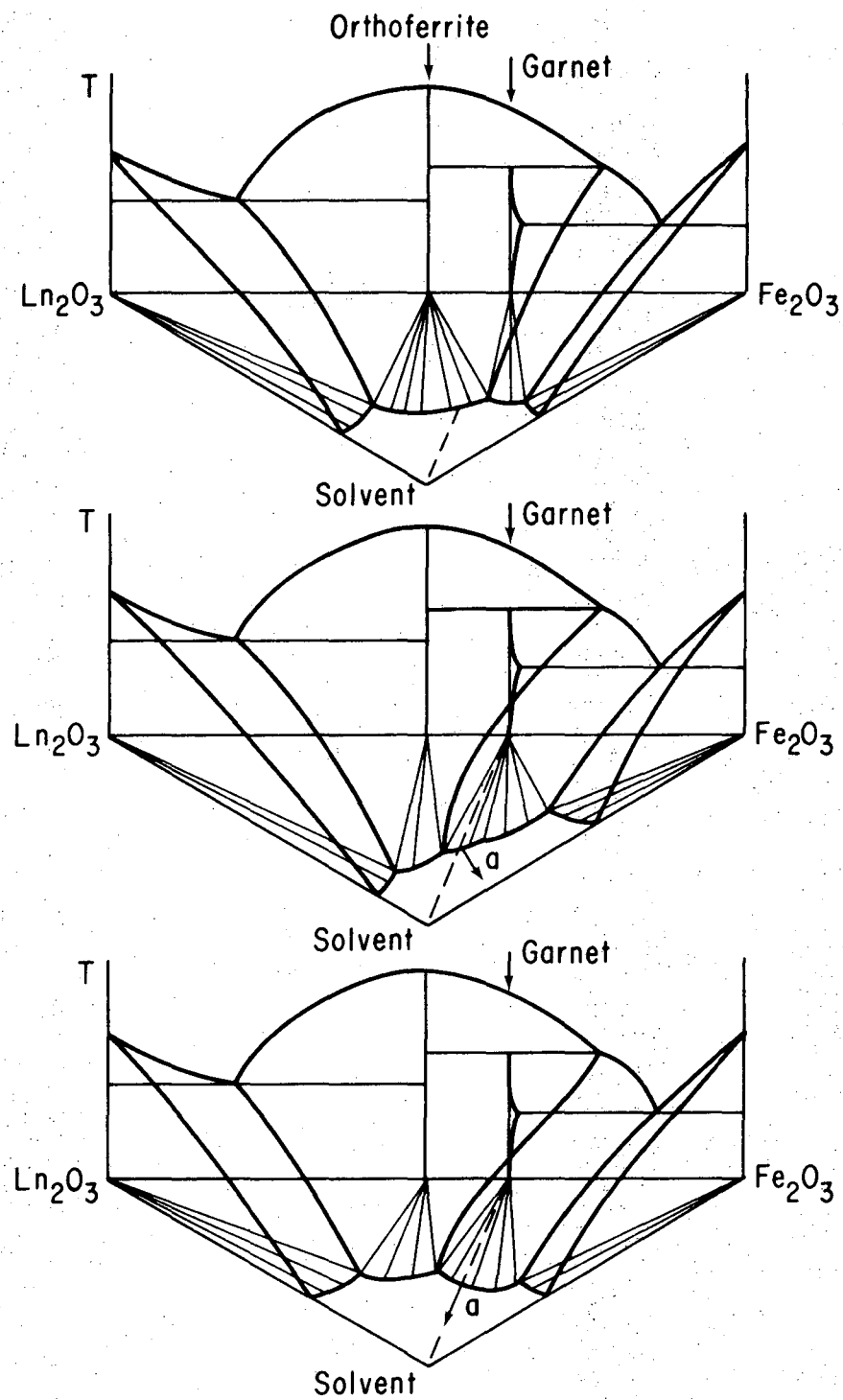
The solvent consisting of 18 mole% PbO in BaO·B<sub>2</sub>O<sub>3</sub> was found to cause higher solvent incorporation in the garnet films when the mole fraction of dissolved garnet was large. The 34 mole% PbO-66 mole% BaO·B<sub>2</sub>O<sub>3</sub> solvent prevented excess iron from becoming incorporated in the garnet films.

These results can be interpreted with the pseudo-ternary phase diagram shown in Fig. 1b. For the solvent containing 26 mole% PbO, the garnet formation region contains the stoichiometrical line only

at large fractions of dissolved garnet. The composition ranges for garnet-liquid phase equilibria for the solvents containing 18 and 34 mole% do not allow congruent saturation of the garnet phase except at low fractions of dissolved garnet.

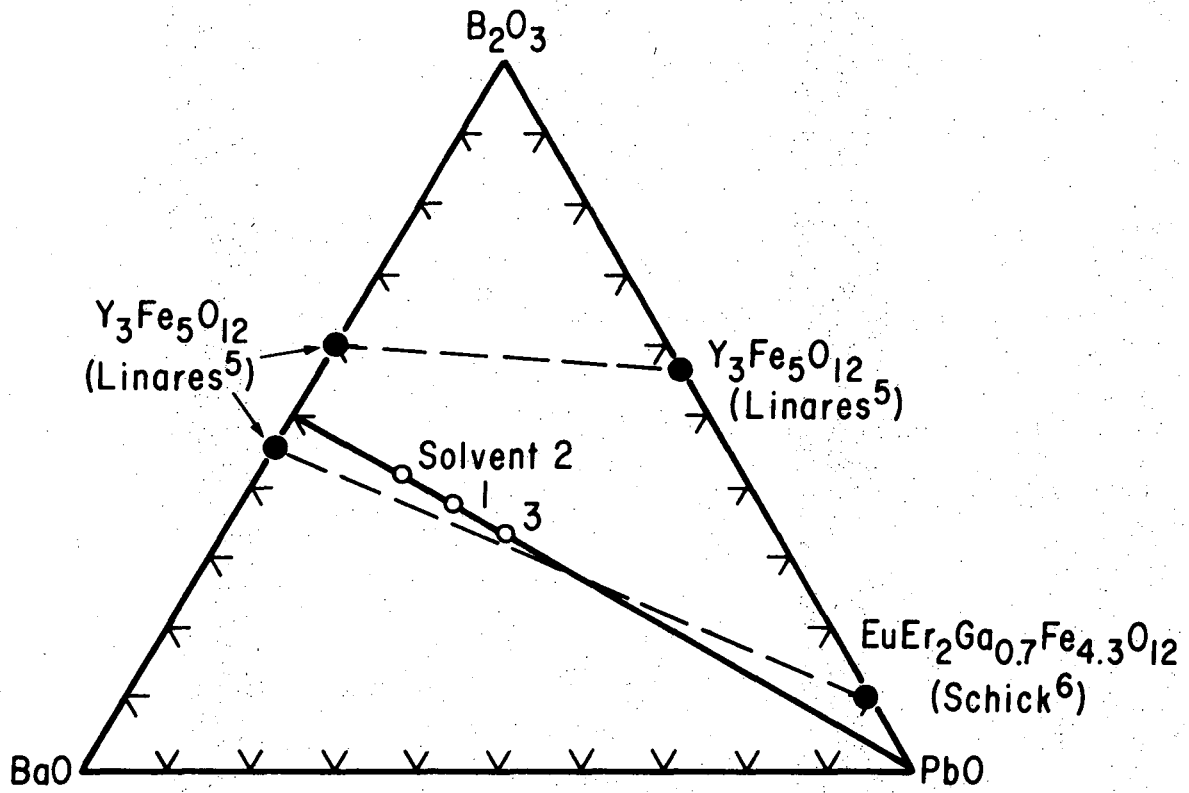
FIGURE CAPTIONS

- Fig. 1. Ternary phase diagram for garnet solution growth: a) non-congruent saturation, b) isothermal congruent saturation, and c) congruent saturation during growth.
- Fig. 2. Region on garnet solution growth in  $\text{PbO-BaO-B}_2\text{O}_3$  solvents.
- Fig. 3. Equipment for liquid phase epitaxial growth of garnet films.
- Fig. 4. Liquidus temperatures for garnet crystal growth for different and iron oxide-rare earth oxide ratios,  $R_1$ .
- Fig. 5. Distribution coefficients of Er and Eu as a function of solvent composition in the  $\text{PbO-BaO}\cdot\text{B}_2\text{O}_3\text{-EuEr}_2\text{Ga}_{0.7}\text{Fe}_{4.3}\text{O}_{12}$  system.
- Fig. 6. Distribution coefficients of as a function of solvent composition in the  $\text{PbO-BaO}\cdot\text{B}_2\text{O}_3\text{-EuEr}_2\text{Ga}_{0.7}\text{Fe}_{4.3}\text{O}_{12}$  system.
- Fig. 7. Distribution coefficients Ba and Pb as a function of solvent composition in the  $\text{PbO-BaO}\cdot\text{B}_2\text{O}_3\text{-EuEr}_2\text{Ga}_{0.7}\text{Fe}_{4.3}\text{O}_{12}$  system.



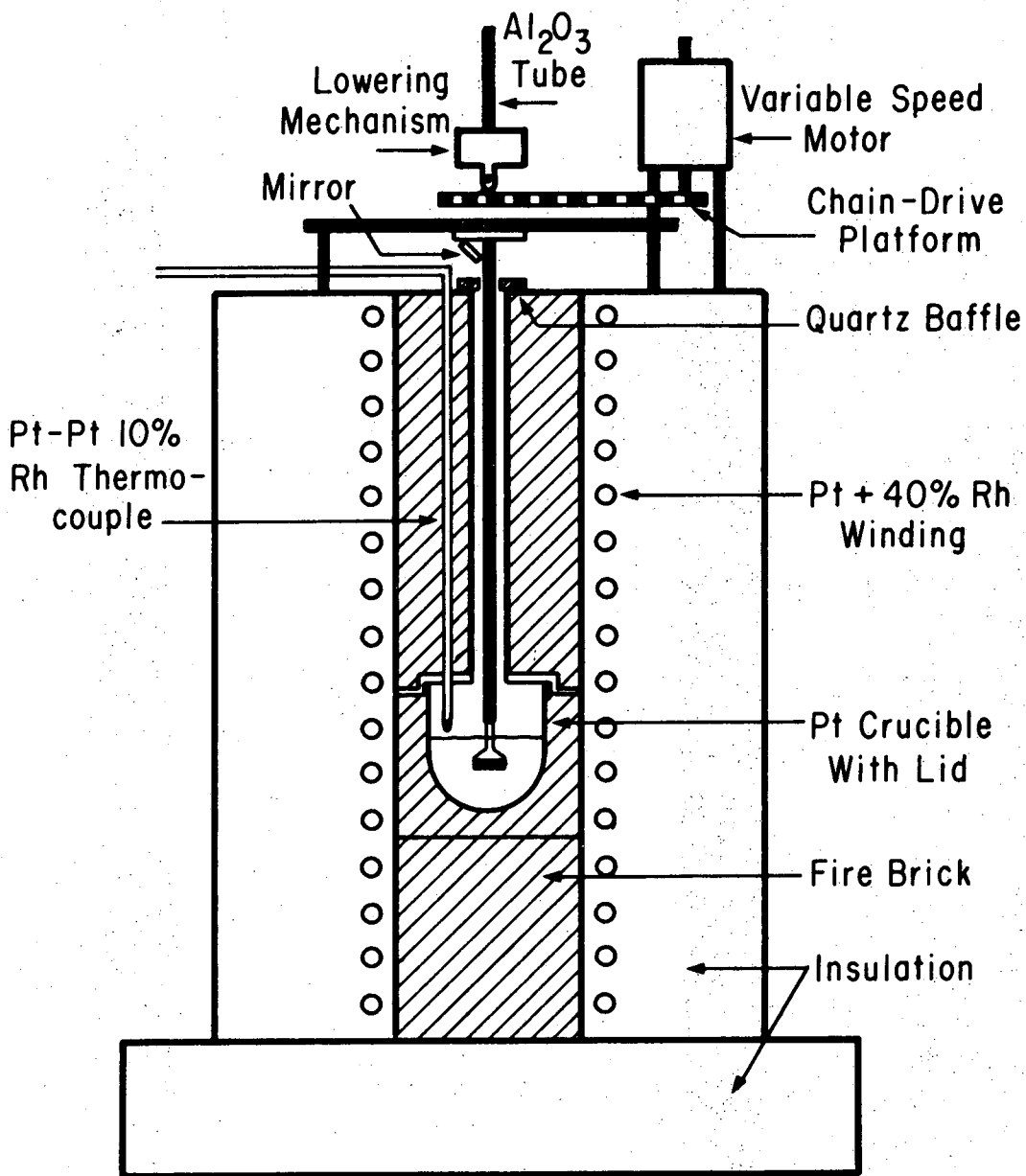
XBL 746-6574

Fig. 1.



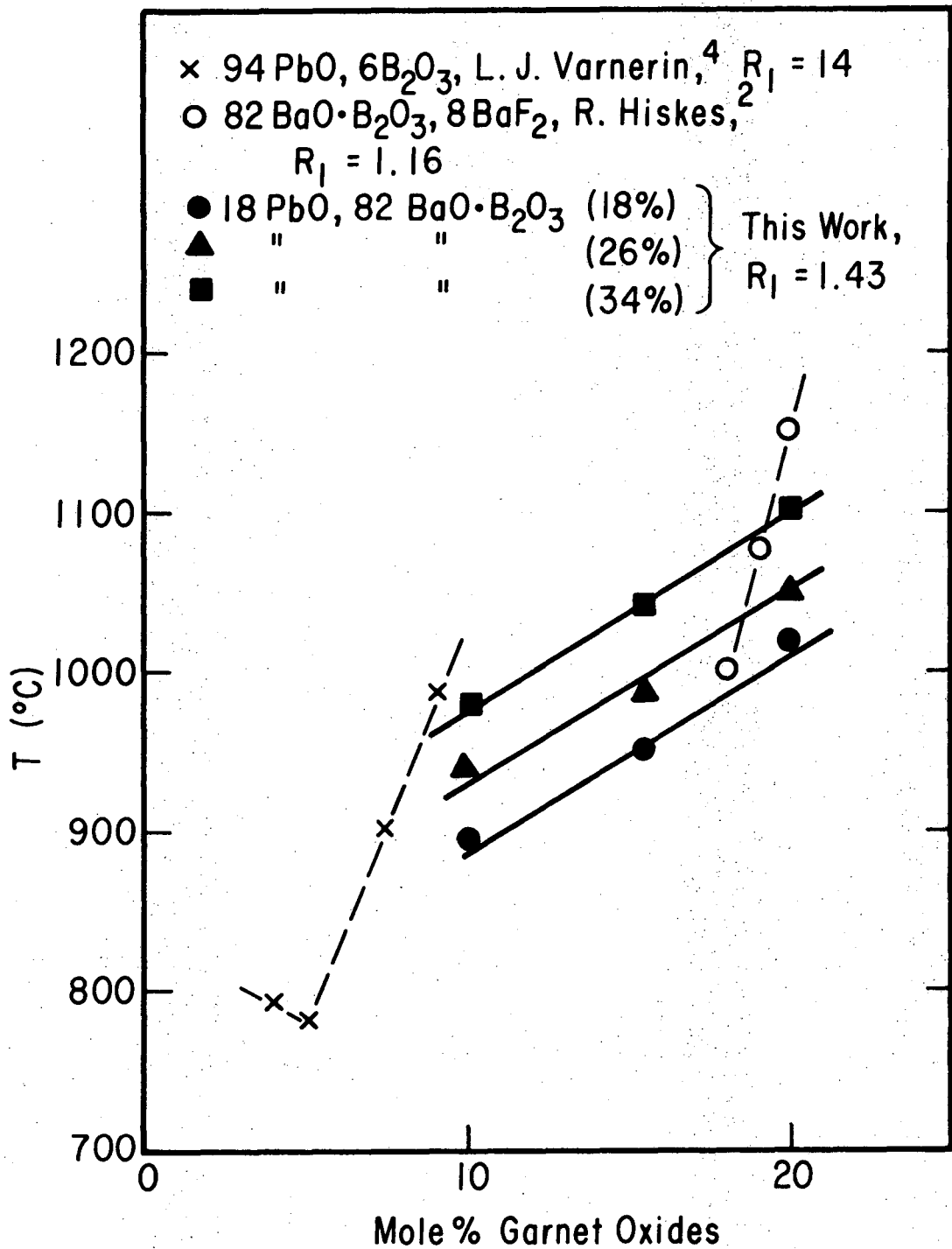
XBL 746-6559

Fig. 2.



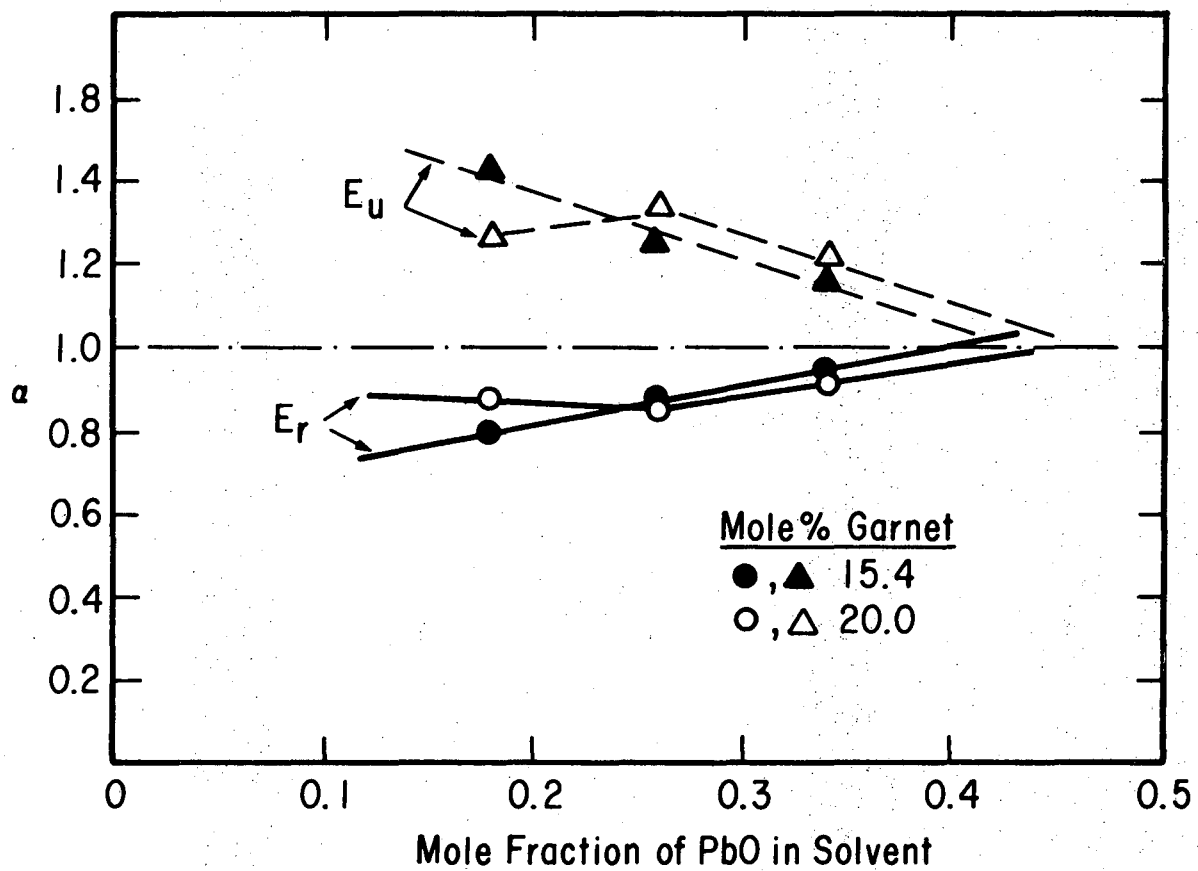
XBL 746-6566

Fig. 3.



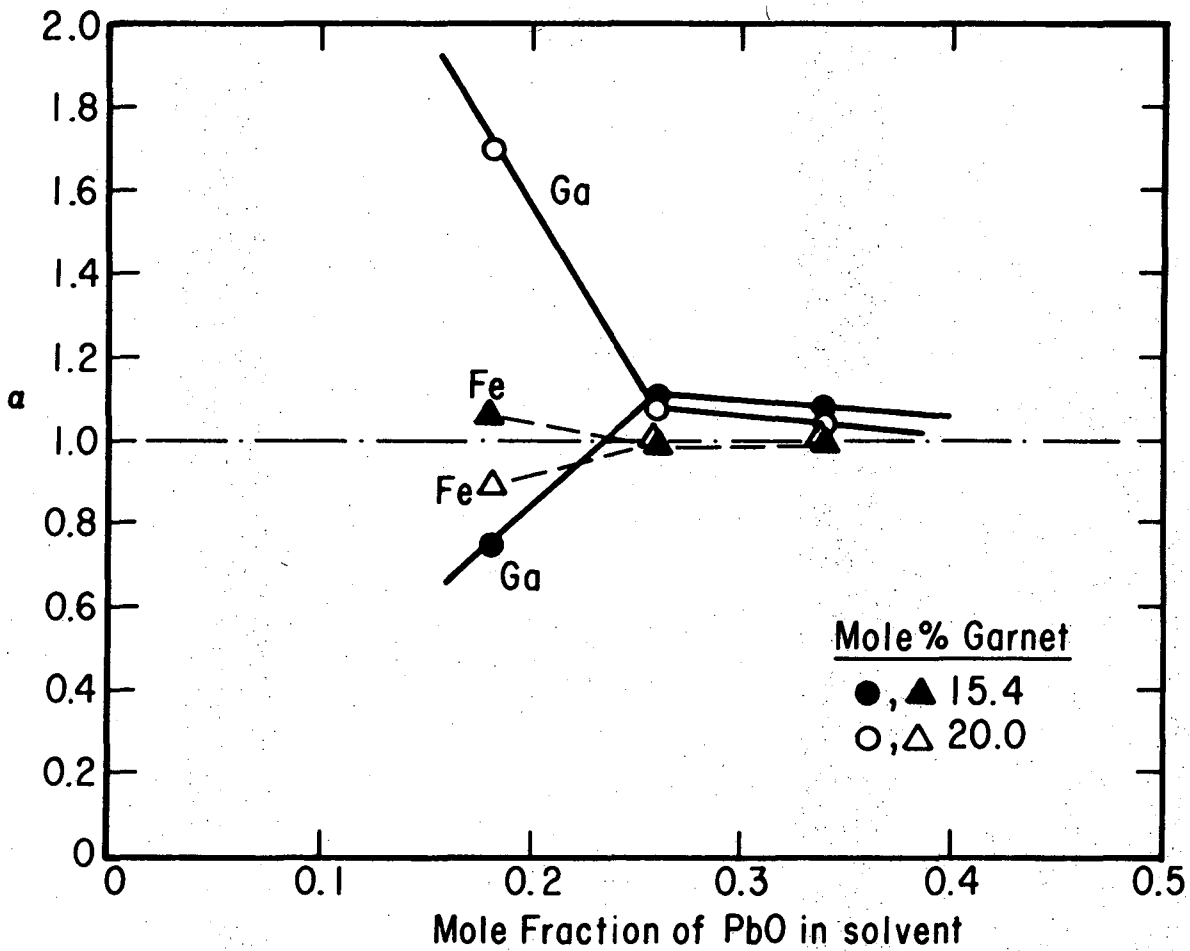
XBL 746-6562

Fig. 4.



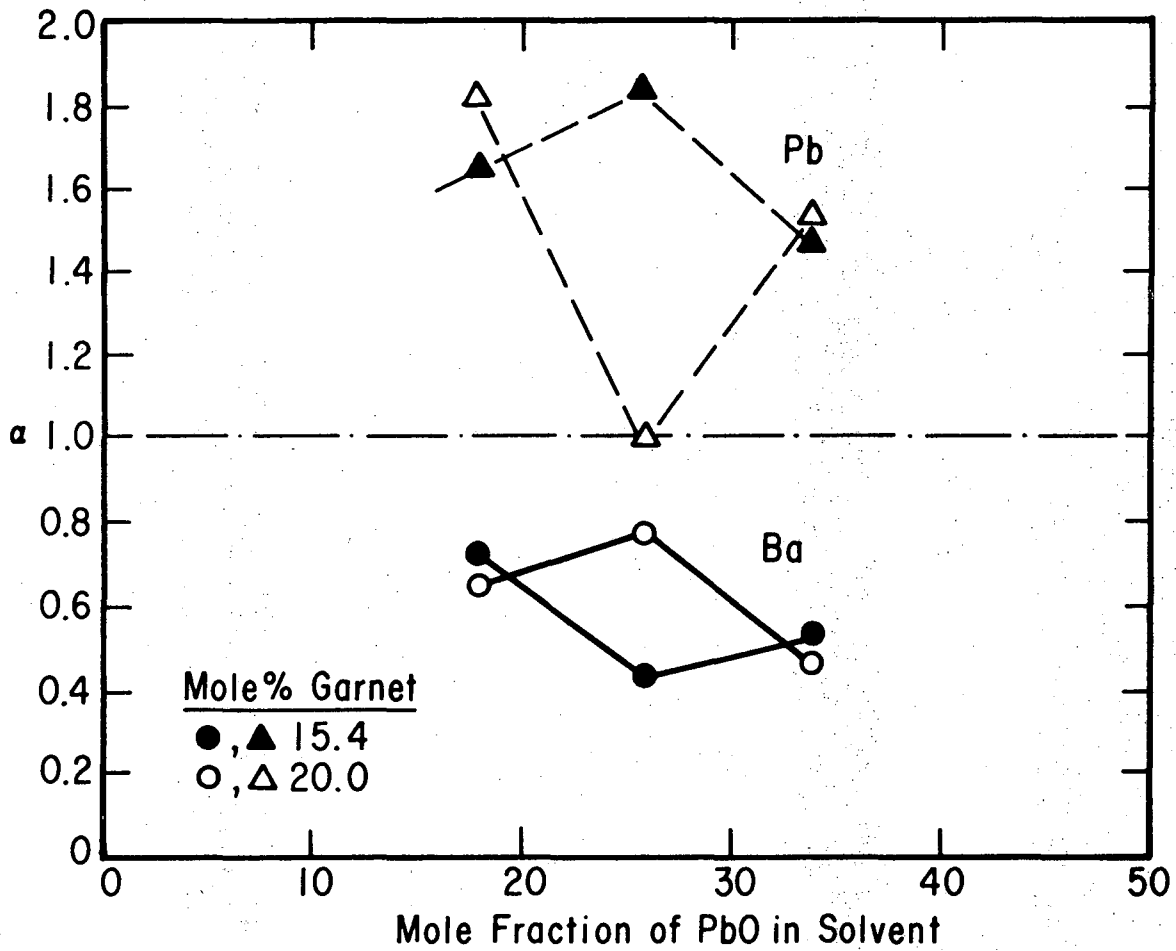
XBL 746-6568

Fig. 5.



XBL 746-6563

Fig. 6.



XBL 746-6564

Fig. 7.

REFERENCES

1. S. L. Blank and J. W. Nielsen, J. of Crystal Growth 17, 302 (1972).
2. R. Hiskes, T. L. Felmlse and R. A. Burmeister, J. Elect. Mat. 1, 458 (1972).
3. J. W. Nielsen, D. A. Lepore and D. C. Leo, "Crystal Growth" proceedings of an International Conference on Crystal Growth, Boston 20-24 June 1966, p. 457.
4. L. J. Varnerin, A perspective on Magnetic Materials for Bubble Mass Memories, p. 329 (1972), Intermag. Conference, Kyoto, Japan.
5. R. C. Linares, J. of the American Ceramic Society 45, 307 (1962).
6. L. K. Shick, J. W. Nielsen, A. H. Bobeck, A. J. Kurtzig, P. C. Michaelis, and J. P. Reekstin, Applied Physics Letters 18, 89 (1972).

## V. GENERAL CONCLUSION

During crystal growth, crystal rotation is an important process for increasing convection, aiding mass transfer and improving the uniformity of components in melt and solution-grown crystals. Crystal rotating for mixing is especially valuable in the Czochralski growth process and in liquid phase epitaxial growth for congruent saturation of the garnet  $\text{EuEr}_2\text{Fe}_{4.3}\text{Ga}_{0.7}\text{O}_{12}$ . Liquid phase epitaxial growth has been studied for solvents in the system  $\text{PbO}-\text{BaO}\cdot\text{B}_2\text{O}_3$ . The highest quality garnet films were grown in a solvent containing 26 mole% PbO in which the garnet oxide mole fraction was 10%. From the result obtained it is concluded that the range of garnet liquid phase equilibria varies slightly with the mole fraction of garnet dissolved in solution. The optimal solvent should be 42 mole% PbO-58 mole%  $\text{BaO}\cdot\text{B}_2\text{O}_3$  in which 10% garnet oxides are dissolved, giving distribution coefficients near unity for all components of the garnet phase.

ACKNOWLEDGEMENTS

To Professor L. F. Donaghey I acknowledge my deepest appreciation for his guidance and constructive criticism. To Professors R. P. Merrill and R. H. Bragg I am grateful for their suggestions in helping me to prepare my final manuscript.

Credit also must be given to Brian Pope for construction of the furnace, George Georgakopoulos for microprobe work, Lee Johnson for sample polishing and Fred Park for his help on use of the electronic equipment.

This work was done under the auspices of the U.S. Atomic Energy Commission.

APPENDIX

Calculation of Molar Ratios in Garnet Films from Microprobe Data

1. Wt. Percentages:

The weight % of each element in a sample was calculated from x-ray counts generated during a ten second period from the sample and from a standard sample. These data must be corrected for the background x-ray intensity. For Er in sample 7 the background intensity was 125 counts/10 sec, and the x-ray intensity correction for background was 3388, while the standard sample containing 2.9 weight % Eu produced 680 counts after background correction. The weight % of Eu was then calculated from the ratio,

$$\frac{\text{Wt\% of Eu in sample 7}}{\text{Wt\% of Eu in standard sample}} = \frac{\text{Counts of Eu in sample 7}}{\text{Counts of Eu in standard sample}}$$

This calculation gives the value,

$$(\text{Wt\% of Eu in sample 7}) = 2.9 \times \left(\frac{3388}{680}\right) = 14.4 .$$

2. Mole Ratio

When the weight % of each element had been calculated, the mole ratio was next calculated. In sample 7, the weight percentages were

14.4 Eu, 33.1 Er, 30.9 Fe, 2.07 Ga, 1.00 Ba and 4.30 Pb.

After dividing these values by their own atomic wt. one obtains the mole percentages, 0.095 Eu, 0.20 Er, 0.55 Fe, 0.03 Ga  $7.28 \times 10^{-3}$  Ba and 0.21 Pb. These elements are thus present in the ratio,

Eu : Er : Fe : Ga : Ba : Pb ::

0.841 : 1.770 : 4.869 : 0.266 : 0.065 : 0.186 .

The recorded x-ray intensities for different samples is summarized in Table A-1. In Table A-2 the standard counts and composition of the standard sample are given. The computed weight percentages of elements in the garnet film are given in Table A-3. Calibration curves for the six elements were then constructed for the solutions used for film growth, after correction for background. These shown in Figs. A-1 through A-6 were used to check the data for internal consistency. The systematic error for Eu and Ga were relatively high. Data for Eu, Ba and Ba showed a high degree of internal consistency.

Table A-1. X-ray Counts for each Element.

Sample	Counts/10 sec.					
	Eu	Er	Ga	Fe	Ba	Pb
1	3450	5760	1712	11512	133	30
2	3736	4936	1114	11244	164	12
3	3295	6153	1757	12090	203	42
7	3438	5190	1534	9949	84	7
8	1720	5070	2926	8680	133	11
9	3435	6257	1752	11998	84	39

These data have been corrected for backgrounds which are Eu(125) Er(120) Ga(1016) Fe(110) Ba(1028), Pb(230)

\* The values for Boron are not shown here, since this element is difficult to detect by electron microprobe analysis.

† The films of samples 4.5, 6 were too thin to examine by electron microprobe analysis.

Table A-2. The standard counts and composition of the standard sample.\*

Element	Eu	Er	Ga	Fe	Ba	Pb
Total counts	1000	1000	1000	1000	1000	1000
wt% as oxide	7.50	7.02	4.53	3.10	1.00	21.68

\*Solution crystallized around sample 6.

Table A-3. The wt% of each element in garnet film.

Sample	Eu	Er	Fe	Ga	Ba	Pb
1	25.88	40.44	7.75	33.96	0.13	0.67
2	28.02	34.61	5.04	34.86	0.16	0.26
3	24.71	43.2	7.95	34.72	0.20	0.91
7	25.79	36.43	6.94	30.84	0.08	0.15
8	20.40	30.50	10.39	26.91	0.13	0.24
9	25.76	43.92	7.93	37.17	0.08	0.41

FIGURE CAPTIONS

Fig. A-1. Calibration curve of Eu.

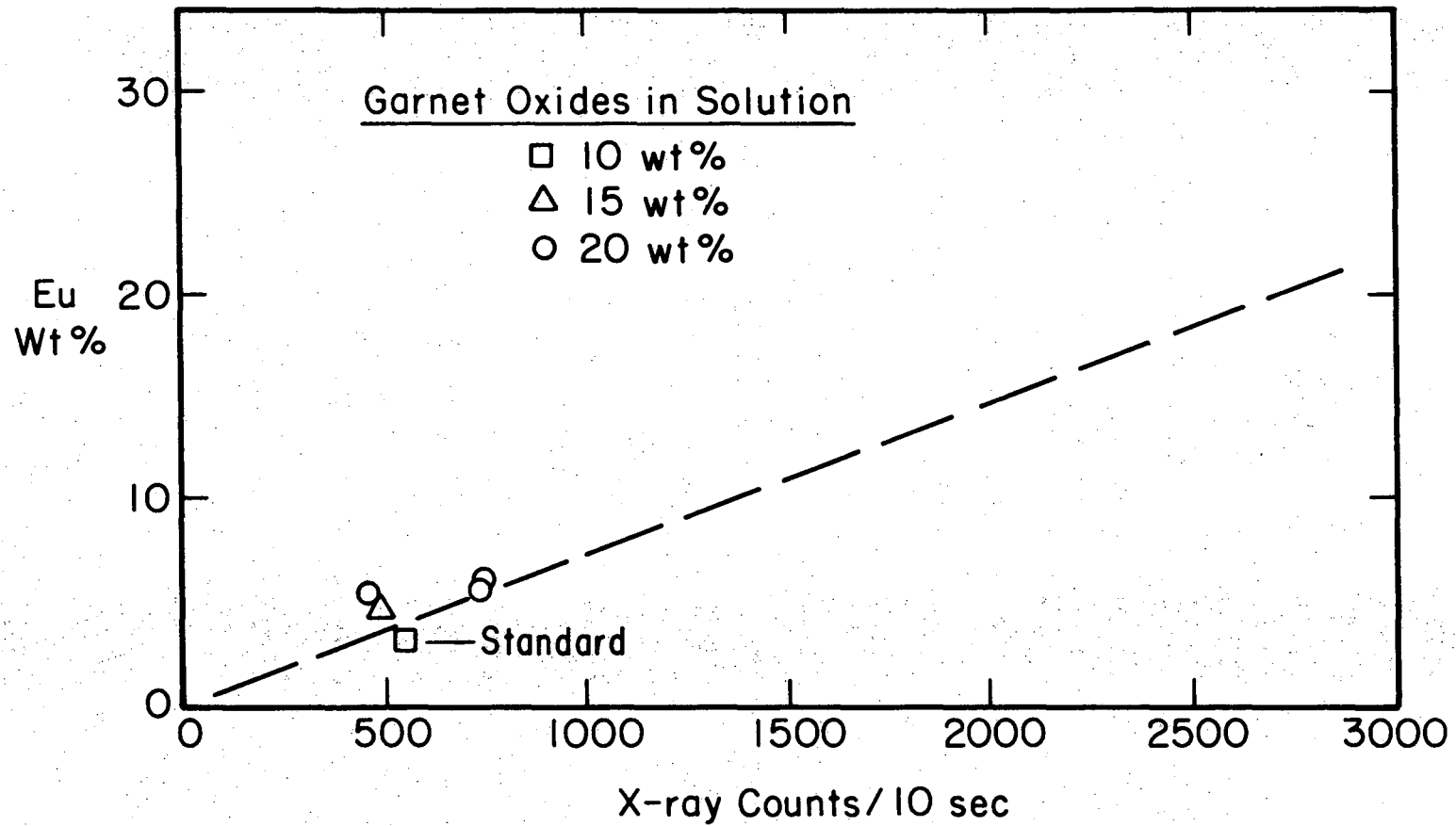
Fig. A-2. Calibration curve of Er.

Fig. A-3. Calibration curve of Ga.

Fig. A-4. Calibration curve of Fe.

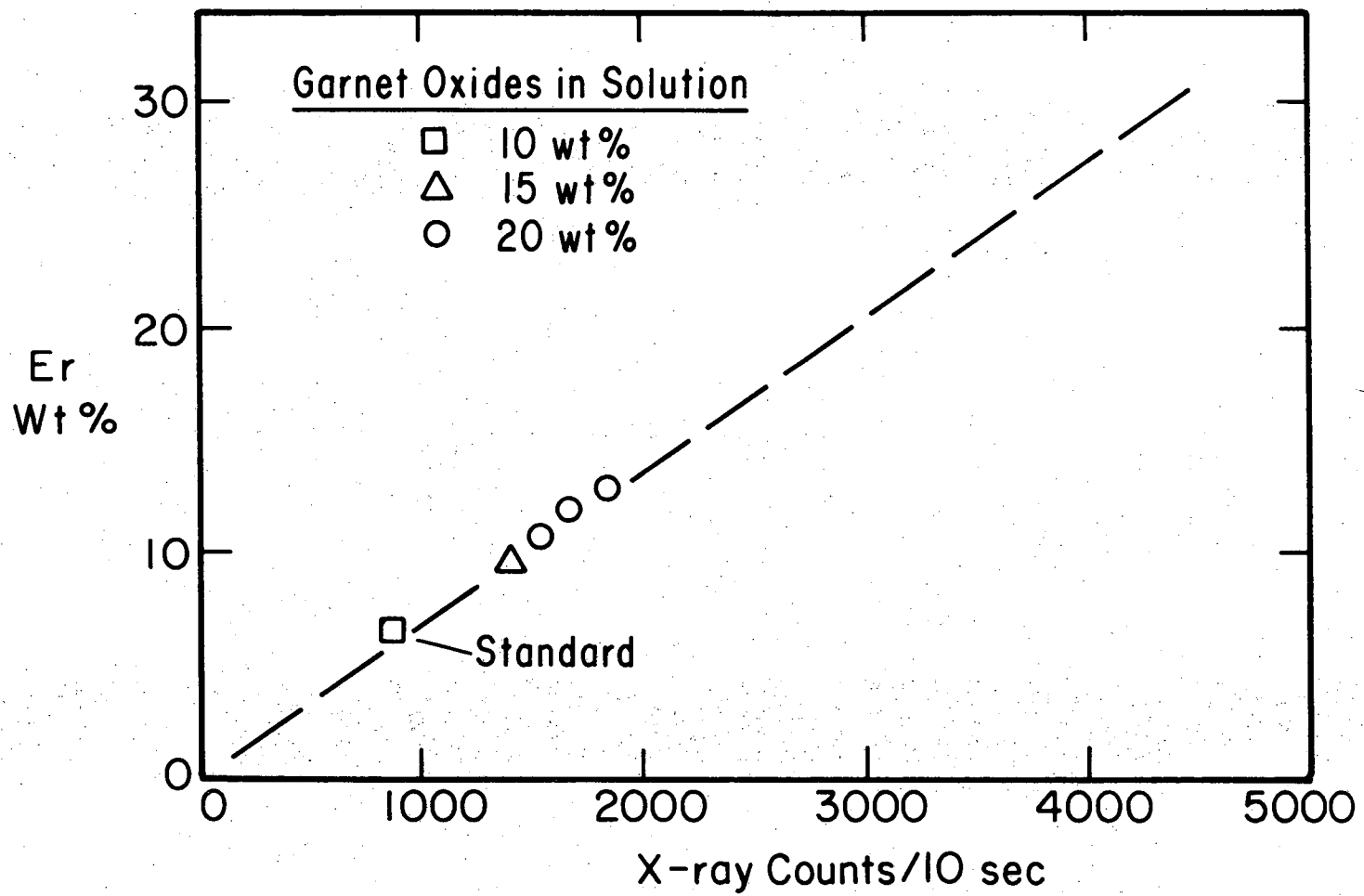
Fig. A-5. Calibration curve of Ba.

Fig. A-6. Calibration curve of Pb.



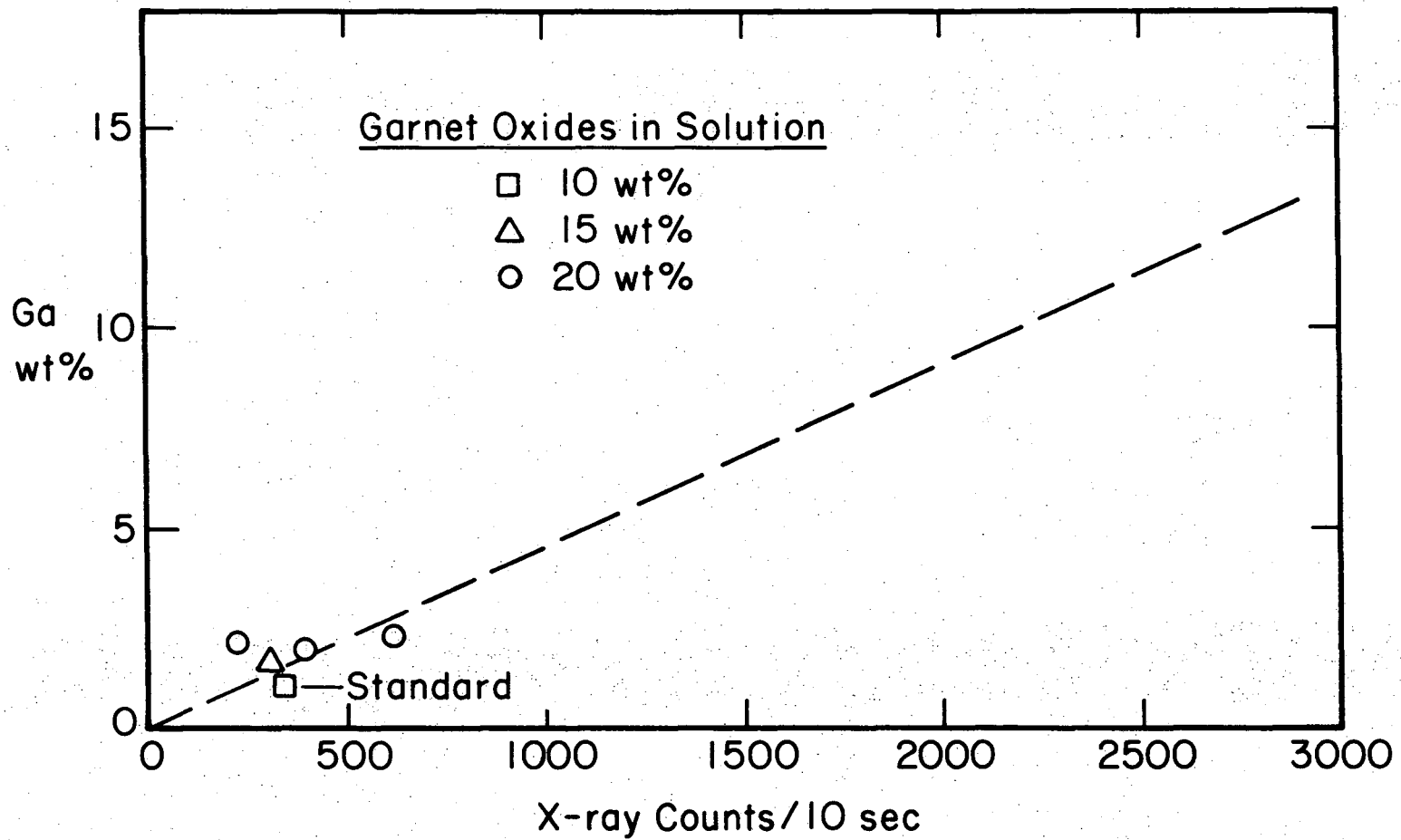
XBL 746-6569

Fig. A-1.



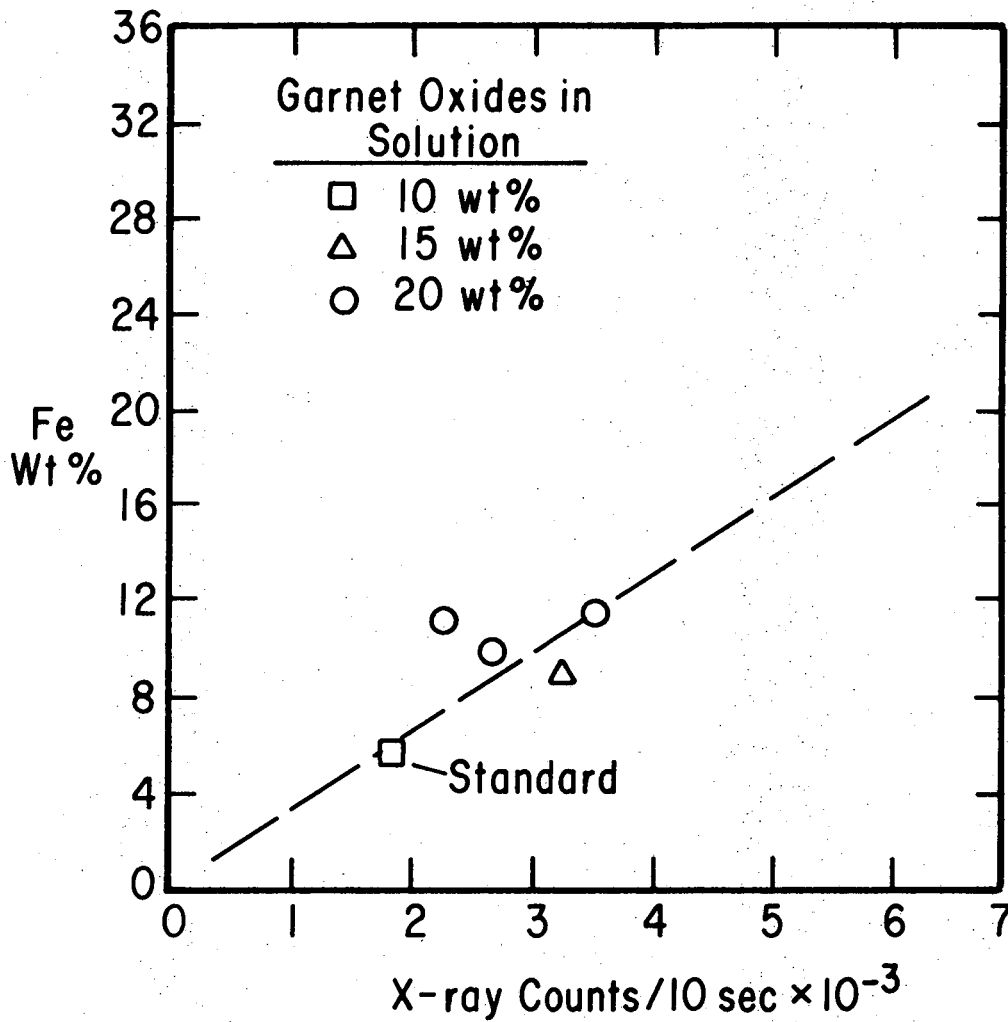
XBL 746-6570

Fig. A-2.



XBL 746-6572

Fig. A-3.



XBL 746-6571

Fig. A-4.

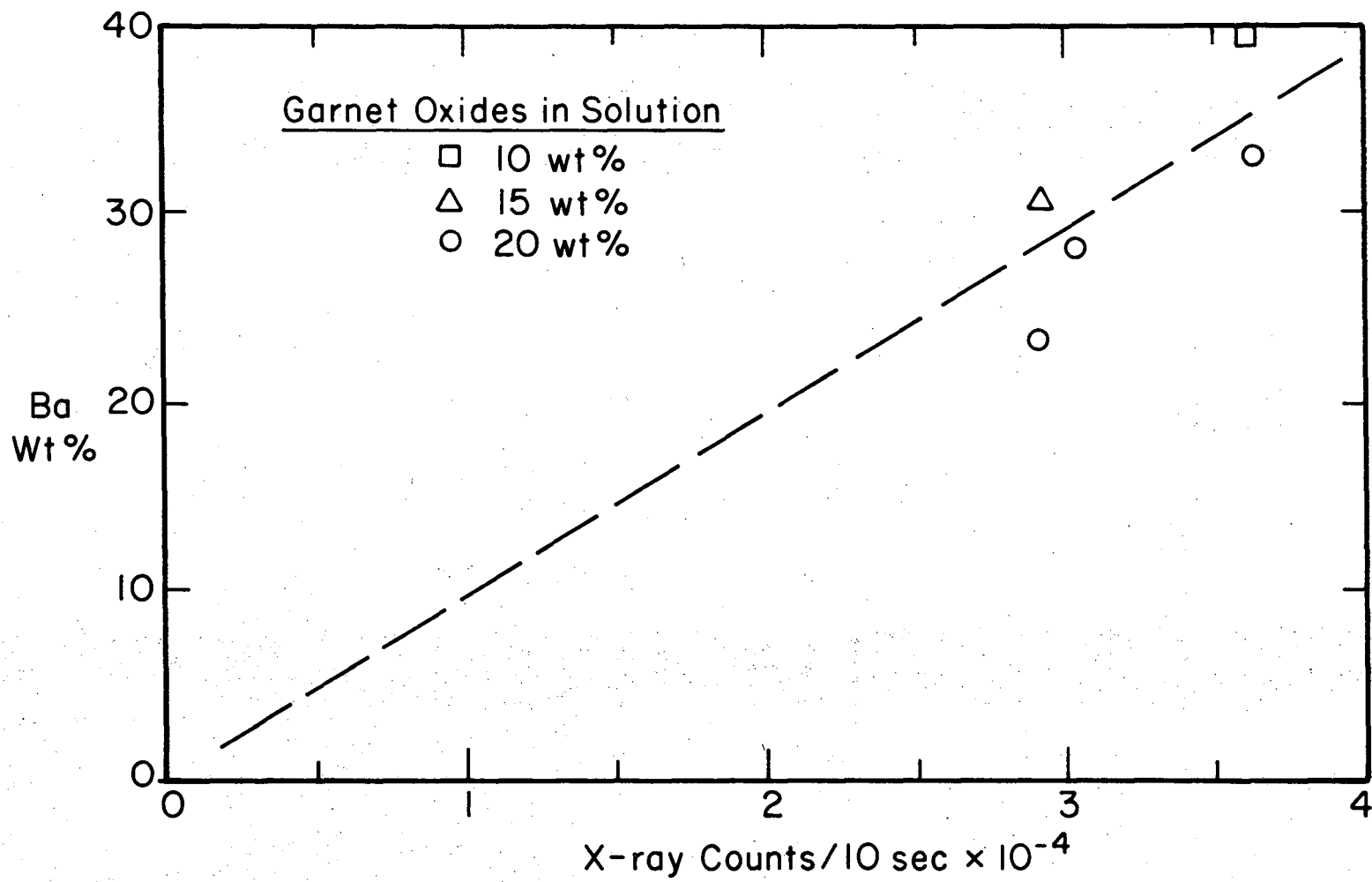
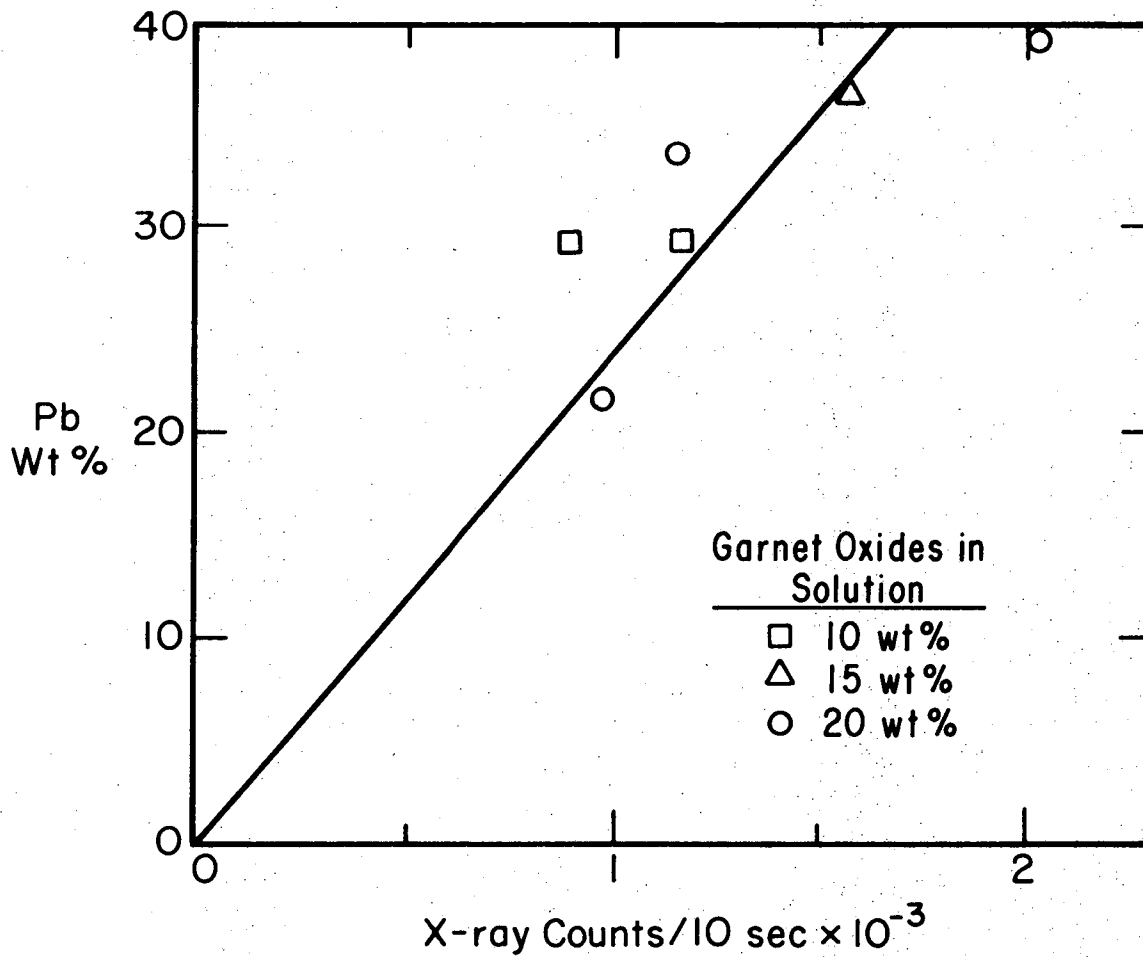


Fig. A-5.

XBL 746-6576



XBL 746-6575

Fig. A-6.

LIST OF SYMBOLS

d	fluid density ( $\text{gm/cm}^3$ )
F	dimensionless radial flow velocity
G	dimensionless tangential flow velocity
H	dimensionless axial flow velocity
p	pressure ( $\text{dynes/cm}^2$ )
P	dimensionless dynamic pressure
L	Height of liquid contained in the crucible (cm)
$N_R$	Rossby number
$N_T$	Taylor number
$R_1$	radius of crystal (cm); component ratio
$R_2$	radius of crucible (cm)
$S_c$	Schmidt number, $\nu/D$
$\bar{v}$	mass average velocity
z	normal distance from the crucible bottom plane
$\alpha$	distribution coefficient
$\Gamma(4/3)$	the gamma function of 4/3, = 0.89298
$\theta$	angular velocity co-ordinate
$\mu$	rotational velocity ratio ( $\Omega_2/\Omega_1$ )
$\nu$	kinematic viscosity ( $\text{cm}^2/\text{sec}$ )
$\rho$	radii ratio ( $R_2/R_1$ )
$\sigma$	reduced fluid height ( $L/R_1$ )
$\tau$	viscous stress ( $\text{dynes/cm}^2$ )
$\Omega_i$	angular velocity of surface i (radians/s)

NOMENCLATURE (Cont.)

$$\text{Pearson} = L \begin{cases} \rightarrow \Omega_2 \\ \rightarrow \Omega_1 \end{cases}$$

$$R \equiv \frac{L^2 \Omega_0}{\nu} \quad \text{solutions for } \begin{cases} \Omega_2 = 0 \\ \Omega_1 = 1 \end{cases},$$

$$\begin{cases} \Omega_2 = -1, -.9, -.5, -.25, -.1, -.04 \\ \Omega_1 = 1 \end{cases}$$

$$\text{Us} = L \begin{cases} \xrightarrow{R_1} \Omega_1 \geq 0 \\ \xrightarrow{R_2} \Omega_2 \geq 0 \end{cases}$$

$$\text{Reynold's No.} = \omega_1 = \frac{\Omega_1 R_1^2}{\nu}$$

$$\omega_2 = \frac{\Omega_2 R_2^2}{\nu}$$

$$\omega_{iL} = \frac{\Omega_i L^2}{\nu}$$

$$\eta = \frac{R_1}{R_2} = \frac{1}{2} \text{ or } \frac{1}{3}$$

$$= \frac{L}{R_2} = \frac{1}{2} \text{ or } \frac{1}{3}$$

LEGAL NOTICE

*This report was prepared as an account of work sponsored by the United States Government. Neither the United States nor the United States Atomic Energy Commission, nor any of their employees, nor any of their contractors, subcontractors, or their employees, makes any warranty, express or implied, or assumes any legal liability or responsibility for the accuracy, completeness or usefulness of any information, apparatus, product or process disclosed, or represents that its use would not infringe privately owned rights.*

TECHNICAL INFORMATION DIVISION  
LAWRENCE BERKELEY LABORATORY  
UNIVERSITY OF CALIFORNIA  
BERKELEY, CALIFORNIA 94720